Mechanistic interactions in polymer electrolyte fuel cell catalyst layer degradation

Navneet Goswami[1,a], Jonathan B. Grunewald[2,b], Thomas F. Fuller[2,c], Partha P. Mukherjee[1,d,*]

[1]School of Mechanical Engineering, Purdue University, West Lafayette, IN 47907, United States

[2]School of Chemical and Biomolecular Engineering, Georgia Institute of Technology, Atlanta, GA 30332, United States

*Corresponding author: pmukherjee@purdue.edu (P. P. Mukherjee)

[a] ORCID: 0000-0001-6512-0749
[b] ORCID: 0000-0003-3094-2528
[c] ORCID: 0000-0001-5474-2876
[d] ORCID: 0000-0001-7900-7261

Abstract:

Polymer Electrolyte Fuel Cells (PEFCs) exhibit considerable performance decay with cycling owing to the degradation of platinum (Pt) catalysts, resulting in the loss of valuable electrochemically active surface area. Catalyst inventory retention is thus a necessity for sustained cathodic oxygen reduction reaction (ORR) and to ameliorate the life expectancy of the PEFC. We demonstrate a thermo-kinetic model cognizant of processes like platinum particle dissolution-reprecipitation and oxide formation coupled with an electrochemical reactive transport model to derive mechanistic insights of the deleterious phenomena at the interfacial scale. The heterogeneous nature of particle aging in a catalyst layer environment is delineated through coarsening-shrinking zones and further comprehension about instability signatures are developed from the dissolution affinity of diameter bins through a metric, onset time. The severe degradation at high temperature and fully humidified conditions is intertwined with the local transport resistance and the critical transient where the catalyst nanoparticles reach a limiting diameter stage. We further reveal the degradation-performance characteristics through variation in the ionomer volume fraction and the mean size of the particle distribution in the electrode. It has been found that the kinetic and transport characteristics are crucially dependent on the interplay of two modes – one leading to the depletion of the catalyst nanoparticles and the other that emanates from catalyst coarsening.

Keywords: thermo-kinetic; dissolution-reprecipitation; oxide formation; onset time; instability; catalyst depletion; coarsening

TOC graphic:

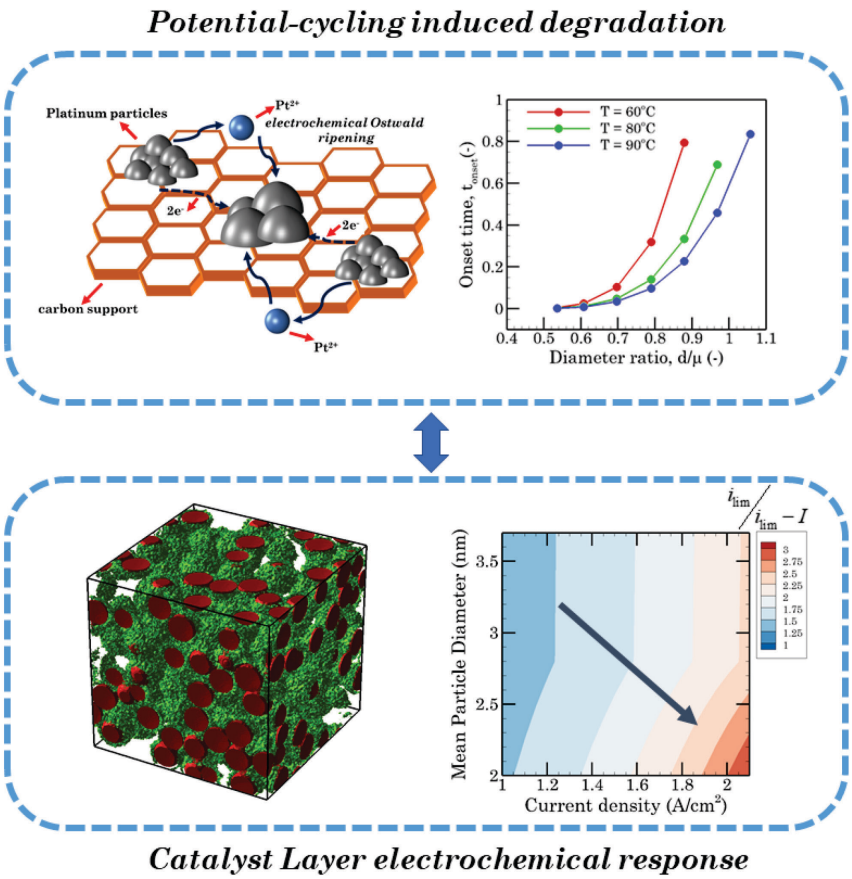
Potential-cycling induced degradation
Platinum particles
Pt²⁺
electrochemical Ostwald ripening
2e⁻
2e⁻
carbon support
Pt²⁺
T = 60°C
T = 80°C
T = 90°C
Onset time, t_onset (-)
Diameter ratio, d/μ (-)
Mean Particle Diameter (nm)
Current density (A/cm²)
Catalyst Layer electrochemical response

I. Introduction:

Hydrogen being a zero-carbon energy carrier[1] is paramount towards creating a long-term, sustainable ecosystem that can tackle the depletion in fossil reserves as greenhouse emissions continue to surge. Rapid strides are already in place in this regard with the Department of Energy's recent announcement to minimize the cost associated with clean hydrogen to $1/ kg in a decade[2]. Propelling a hydrogen-based energy infrastructure is an enabler in unlocking and expanding its usage in a wide spectrum of markets including heavy-duty vehicles, aviation, and marine transport, metal refining, and industrial processes that deliver chemical feedstock like ammonia etc[1]. In this context, Polymer Electrolyte Fuel Cells (PEFCs) can serve several potential applications in the form of light-duty passenger vehicles, buses, trucks as well as stationary power systems which can be ascribed to its environmentally benign nature with zero emissions, scalability, high conversion efficiency and low noise operation[3–6]. Nanometer-sized catalyst particles containing platinum (Pt) are dispersed in the catalyst layer to boost the efficiency of the otherwise sluggish oxygen reduction reaction (ORR). However, the catalyst particles come along with a caveat of intrinsic instability[7,8] which makes them prone to dissolution. As such, PEFC technology is plagued with durability challenges in addition to the cost constraints[9] associated with the platinum group metal catalysts. Under the exposure to dynamic and idling conditions, a PEFC suffers from a loss in the electrochemical active area (ECA) and valuable catalyst inventory which leads to an impediment in its long-term performance. It is observed that the participating aging mechanisms manifest through: (a) Electrochemical Ostwald Ripening on carbon support, (b) detachment of catalyst particles induced by carbon corrosion, (c) Pt crystal migration and coalescence, and (d) Pt dissolution, ion transport through the ionomer phase and subsequent reprecipitation to form a band in the

membrane. The degradation mechanisms that occur in an operating environment along with its challenges, opportunities, and material evolution have been summarized in recent review articles[10–13].

Under the application of a durability protocol, the impact of several stressors such as temperature[14], relative humidity[15], partial pressure[16,17], pH[18], oxygen[19,20], particle sizes[8,21] on accelerating the long-term degradation process has been extensively reported in a series of experimental works. Harzer et al.[22] performed durability tests for a cathode with varying loadings under the exposure to different waveforms of the accelerated stress tests (ASTs) - square, triangular and analyzed its consequent effect on voltage cycling induced degradation. The design of the cycling profile from the context of scan and dwell rates pertaining to the ASTs and its consequent influence on the ECA loss has been investigated in Kneer et al.[23] Both the works reported that the square waves led to a rapid drop in the ECA compared to triangular waves owing to the comparatively longer hold times at the upper potential limit in the former. Furthermore, it was observed that the degradation rates per voltage cycle escalated at lower scan rates, however, the rates when normalized to operating time were invariant when tested over the extent of scan rates for triangular wave voltage cycling. High operational temperatures resulted in an elevated extent of catalyst degradation as more Pt inventory was deposited in the membrane along with a significant loss in the ECA[14]. Bi et al.[15] probed the effect of relative humidity (RH) and attributed the increase in catalyst degradation at high RH to the enhanced platinum ion diffusion through the water transport pathways in the polymer electrolyte. In addition, it was found that the oxygen partial pressure did not have any contribution in triggering the degradation process. Studies conducted by Bi et al.[16] and Zhang et al.[17] however highlighted

that the Pt reprecipitation within the membrane – a crucial adverse mechanism bears a strong dependence on the hydrogen (anode) and oxygen (cathode) partial pressures. Mitsushima et al.[18] determined the Pt solubility in acidic electrolytes and found it to increase with high temperature and decrease in higher pH. The existence of oxygen in an acidic electrochemical media resulted in increased platinum dissolution even at lower potentials and was demonstrated by Matsumoto et al.[19] The particle size effect on platinum dissolution was elucidated in a couple of works by Sandbeck et al.[8,21] Nanoparticles with the same loading but varying particle sizes were synthesized via the two-step surfactant-free toolbox approach. Decreasing stability was observed at smaller particle sizes with transition in the onset of anodic dissolution and oxide formation towards more negative potentials. A trade-off between particle-size dependent change in oxophilicity and ECA was further portrayed that must be taken into consideration while designing ASTs.

A mechanistic elaboration of the governing processes supported through imaging evidence of the catalyst aging was presented in [7,24–26]. Dubau et al.[25] utilized several physicochemical analytical techniques to reveal the heterogeneous trend of aging within a membrane electrode assembly (MEA) under different operating conditions. It was depicted that the cathode inlet aged quickly in comparison to that of the outlet at significantly high cell currents. Kneer et al.[26] visualized the microstructural changes in degraded MEAs through characterization tools and inferred correlations with kinetic overpotentials and oxygen transport resistances. In this regard, attention must also be brought to effective suppression strategies to curb dissolution by means of interfacial-scale redesign and material modification as has been highlighted in a few recent works[27–32]. Some notable studies that proved to ameliorate the durability manifold include

employing a gold underlayer to the electrocatalyst at the atomic scale[27]; usage of mesoporous cathode electrocatalysts[29]; composite support-based catalysts[30]; polybenzimidazole-coated graphene-based fuel cell catalysts[31]. To further the endeavor in improving the device sustainability, development is also under progress to engineer catalysts with nanocellulose-based materials[32] that can provide cost-effective solutions in addition to possessing appreciable activity and durability.

Mathematical modeling has been aptly harnessed to aid the experimental reports to facilitate the assessment of the fundamental driving mechanisms[33–48]. The earlier investigation includes that of Darling and Meyers[33] who were the first to formulate kinetic rate expressions for electrochemical Pt dissolution, Pt oxide film formation, and Pt oxide chemical dissolution. Holby et al.[35] developed a model to delineate the signature of varying particle size distributions (PSDs) and crossover hydrogen on the catalyst degradation process. They further advanced the model to accommodate the detailed thermo-kinetics description of the Pt dissolution/precipitation reaction and the oxide formation/removal reaction[36]. A one-dimensional model was developed by Li et al.[37] for a cathode catalyst layer which further took into account the transient diffusion of Pt^{2+} ions through the ionomer that ultimately leads to the formation of a platinum band. To further decrease the computational expense that is inherently associated with a long-term cycling model, Schneider et al.[38] proposed a 0-D empirical model that also simulated the effects of carbon corrosion and place-exchange mechanisms. In a couple of works, Zheng et al.[39] utilized the thermo-kinetic modeling approach to probe the effect of waveform, scan rate, cycle duration, and dwell time at the upper potential limit (UPL) and additionally explored the design of a graded catalyst layer[40] as a mitigation strategy to curb voltage cycling induced degradation.

To this end, it has been observed that computational models that can simulate both catalyst degradation mechanisms along with further elucidating its consequent impact on the electrochemical response are quite scarce. In this work, we aim to bridge that gap and provide a mechanistic evaluation at the confluence of three decisive aspects of a catalyst layer – its architecture, electrochemical response, and long-term durability. Our scale-bridging mesoscale model reveals the instability associated with degradation in addition to shedding light on the microstructural attributes to degradation-performance interactions. The analysis has been performed to explore the influence of a host of parameters – temperature, relative humidity, ionomer volume fraction, mean particle size, oxide-oxide interaction energy. The heterogeneous fingerprint of catalyst aging is exhibited which is further demarcated into shrinking and coarsening zones that help deconvolute the contribution of mechanisms that lead to the decay in the valuable electrochemical active area. A transient metric, onset time is introduced which is cognizant of the complete dissolution of the particles to a limiting diameter.

2. Mathematical Description:

(i) Degradation model:

The concomitant degradation mechanisms at play under a favorable electrochemical environment are highlighted schematically in Figs. 1(a-c). A differential in the interfacial energy drives Ostwald Ripening[24,49] (Fig. 1(a)) where the platinum catalysts dissolve from particles having a smaller diameter and again redeposit on larger particles to attain a more stable configuration. The carbon support which serves as a host to the catalyst nanoparticles fosters the percolation of electrons and bears a complicated, hybridized structure; however, it has been depicted in a much

more simplistic manner in the schematic. We express the electrochemical reaction for Pt dissolution/ redeposition as:

$$\mathrm{Pt} \rightleftharpoons \mathrm{Pt}^{2+} + 2\mathrm{e}^{-} \left(U_1^{eq} = 1.188\,V\right) \quad (1)$$

There is a propensity of a passivating layer of platinum oxide being formed over the bare surface of the catalyst particles which leads to a reduction in the active area as seen in Fig. 1(b). The reaction for reversible oxide formation and removal is written as:

$$\mathrm{Pt} + \mathrm{H_2O} \rightleftharpoons \mathrm{PtO} + 2\mathrm{H}^{+} + 2\mathrm{e}^{-} \left(U_{fit} = U_2^{eq,0} = 0.98\,V\right) \quad (2)$$

In addition, the dissolved Pt^{2+} ions as shown in Fig. 1(c) can diffuse under a concentration gradient and further interact with crossover hydrogen leading to reprecipitation thereby forming a Pt band in the membrane side. The corresponding reaction is shown below:

$$\mathrm{Pt}^{2+} + \mathrm{H_2} \rightleftharpoons \mathrm{Pt} + 2\mathrm{H}^{+} \quad (3)$$

It has been reported in the literature that the oxidation of Pt atoms does not occur in a single elementary step as seen in Eq. 2 and proceeds via the formation of multiple place-exchanged species at various time instances[20,42], the effect of which has not been taken into account in this study. Also, the chemical dissolution of platinum oxide has been neglected wherein the ion exchange takes place through a chemical pathway as shown below. In fact, from a pure thermodynamics perspective, reaction 2 can be subtracted from reaction 1 to yield reaction 4[33].

$$\mathrm{PtO} + 2\mathrm{H}^{+} \rightleftharpoons \mathrm{Pt}^{2+} + \mathrm{H_2O} \quad (4)$$

Further, Pt degradation originating from carbon corrosion does not place in the range of 0.6 V – 1.0 V for the potential cycling protocols and as such is not considered[37,39].

The catalyst layer modeling domain is pseudo two-dimensional and constitutes the transport direction in x (denoted by subscript i) and discrete diameter bins in the y-direction (denoted by subscript j). The number of control volumes in the x and y direction is designated by N and M respectively. This indicates that on each of the control volumes in i (x-direction), there exist M discrete diameter bins in the y-direction which have been derived from an experimental particle size distribution. The diameter in each particle group is assumed to be lumped and denoted by $d_{i,j}$ while the fractional oxide coverage is referred by $\theta_{i,j}$.

The relevant thermo-kinetic forward and backward reaction rates are based on a modified form of Butler-Volmer kinetics and have been originally formulated by Holby and Morgan[36] and later used by Li et al.[37] and Zheng et al.[39]. To accommodate the size-dependent stability effect of the catalyst particles where the length scale is in nanometers, the Gibbs-Thomson approximation is employed which considered the curvature energetics expressed as a function of the surface tension, molar volume, and diameter. It is worth mentioning here that the Pt particles hosted over the carbon support are hemispherical in shape. The rate expression for Pt dissolution and redeposition (for reaction 1) is as follows:

$$r_{net,Pt^{2+}} = \nu_1 \Gamma \exp\left[\frac{-\overline{H_1}}{RT}\right]\left(1-\min\left(1,\theta_{i,j}\right)\right)\times\left(\begin{array}{l}\exp\left[\dfrac{-n_1F\left(1-\beta_1\right)}{RT}\left(U_1^{eq}-\dfrac{4\Omega_{Pt}\gamma_{Pt}}{d_{i,j}n_1F}-V\right)\right] \\ -\dfrac{\nu_2}{\nu_1}\left(\dfrac{c_{Pt^{2+}}}{c_{Pt^{2+}}^{ref}}\right)\exp\left[\dfrac{n_1F\left(\beta_1\right)}{RT}\left(U_1^{eq}-\dfrac{4\Omega_{Pt}\gamma_{Pt}}{d_{i,j}n_1F}-V\right)\right]\end{array}\right)\times RH^{1.7} \quad (5)$$

In the above expression, ν_1 is the forward reaction attempt frequency, Γ is the surface density of Pt atoms, $\overline{H_1}$ is the partial molar activation enthalpy of the dissolution reaction, n_1 is the number of electrons involved in the reaction (in this case 2), F is the Faraday's constant, β_1 is the charge

transfer coefficient, R is the ideal gas constant, T is the cell temperature, U_1^{eq} is the bulk equilibrium potential, V is the cell voltage, Ω_{Pt} is the molar volume of Pt and γ_{Pt} is the surface tension of Pt. It should be noted that $c_{Pt^{2+}}$ and $c_{Pt^{2+}}$ appearing in the above expression refers to the mean and reference Pt^{2+} concentration respectively. The shift in chemical potential from the bulk Pt $\left(=\frac{4\Omega_{Pt}\gamma_{Pt}}{d_{i,j}n_1F}\right)$ can be attributed to the instability observed in the Pt nanoparticles. The humidity dependence of the Pt dissolution rate[38] has been invoked as a power-law term as seen in Eq. 5.

The rate expression for the reversible formation and removal of the oxide layer (for reaction 2) is defined as:

$$r_{net,oxide}=\nu_1^*\Gamma\exp\left[\frac{-1}{RT}\left(\overline{H_2}+\lambda\theta_{i,j}\right)\right]\times\left(\begin{array}{l}\left(1-\frac{\theta_{i,j}}{2}\right)\exp\left[\frac{-n_2F\left(1-\beta_{2,a}\right)}{RT}\left(U_2^{eq}+\frac{\omega\theta_{i,j}}{n_2F}-V\right)\right]\\-\frac{\nu_2^*}{\nu_1^*}\left(10^{-2\,pH}\right)\frac{\theta_{i,j}}{2}\exp\left[\frac{n_2F\left(\beta_{2,c}\right)}{RT}\left(U_2^{eq}+\frac{\omega\theta_{i,j}}{n_2F}-V\right)\right]\end{array}\right) \quad (6)$$

In the above equation, ν_1^* is the forward rate constant, ν_2^* is the backward rate constant and $\overline{H_2}$ represents the activation barrier when the oxide formation reaction is in equilibrium at zero oxide coverage. It is assumed that the reaction barrier is linearly dependent on the fractional coverage and hence, a prefactor in the form of an oxide kinetic barrier constant, λ is employed. Here, n_2 is the number of electrons transferred (= 2), whereas $\beta_{2,a}$ and $\beta_{2,c}$ indicate the anodic and cathodic transfer coefficients respectively. The oxide-oxide interaction energy is captured through the energy parameter involved in the adsorption of oxygen over the surface of platinum particles and denoted by ω. The term, $\theta_{i,j,vacant}=\left(1-\frac{\theta_{i,j}}{2}\right)$ which represents the fraction of the

platinum surface not covered by oxides, is included in Eq. 6 to allow oxide on the surface to insulate the particle and prevent platinum dissolution from beneath the oxide film. It is worth mentioning that the fitted transfer coefficients in the above rate expression are asymmetric in nature to fit a cyclic voltammogram as highlighted later in Fig. 2(e). The equilibrium oxide potential[33] depends on the particle diameter, $d_{i,j}$:

$$U_2^{eq} = U_{fit} + \frac{1}{F}\left[\frac{\gamma_{PtO}\Omega_{PtO}}{d_{i,j}} - \frac{\gamma_{Pt}\Omega_{Pt}}{d_{i,j}}\right] \tag{7}$$

The transient evolution of the particle diameter groups, and the oxide fractional coverage are governed by Eqs. 8 and 9.

$$\frac{d\left(d_{ij}\right)}{dt} = -r_{net,Pt^{2+}}\Omega_{Pt} \tag{8}$$

$$\frac{d\left(\theta_{ij}\right)}{dt} = \frac{r_{net,oxide}}{\Gamma} - 2\frac{\theta_{ij}}{d_{ij}}\frac{d\left(d_{ij}\right)}{dt} \tag{9}$$

The diffusion of dissolved Pt^{2+} ions through the ionomer phase is given by:

$$\varepsilon_{ionomer}\frac{\partial c_{Pt^{2+}}}{\partial t} = \nabla\cdot\left(\varepsilon_{ionomer}^{1.5} D_{Pt^{2+}}^{ionomer}\nabla c_{Pt^{2+}}\right) + S_{Pt^{2+}} \tag{10}$$

where, $D_{Pt^{2+}}^{ionomer}$ is the diffusivity of Pt^{2+} in the ionomer. In Eq. 10, the effect of Pt^{2+} migration has been neglected based on an order of magnitude analysis as shown by Bi and Fuller[34]. The dependence of $D_{Pt^{2+}}^{ionomer}$ on temperature and relative humidity is included as described in Schneider et al.[38]. The reference temperature (T_{ref}) is considered as 353 K.

$$D_{Pt^{2+}}^{ionomer} = D_{Pt^{2+},ref}^{ionomer} \left(\frac{T}{T_{ref}} \right)^2 RH^2 \tag{11}$$

Under the $H_2|N_2$ (anode | cathode) condition, a Pt^{2+} sink is observed at the membrane-cathode catalyst layer (CCL) interface since the crossover hydrogen flowing from the anode side reaches without any activity with oxygen. The boundary condition can be accordingly written as:

$$c_{\mathrm{Pt}^{2+}}\Big|_{x=0} = 0 \tag{12}$$

However, under $H_2|$Air (anode | cathode) condition, the platinum particles reprecipitate to form a Pt band when exposed to cycling conditions. In such a scenario, the Pt^{2+} follows a linear profile from the membrane-CCL interface to the band. The boundary conditions thus manifest as a mixed type as shown in Eq. 13:

$$\varepsilon_{ionomer}^{1.5} \frac{\partial c_{\mathrm{Pt}^{2+}}}{\partial x}\bigg|_{x=0} = \frac{c_{\mathrm{Pt}^{2+}}}{\delta_{\mathrm{Pt}}} \tag{13}$$

$$\delta_{Pt} = \frac{2K_{\mathrm{O}_2} p_{\mathrm{O}_2} \delta_M}{K_{\mathrm{H}_2} p_{\mathrm{H}_2} + 2K_{\mathrm{O}_2} p_{\mathrm{O}_2}} \tag{14}$$

In Eq. 14, δ_{Pt} represents the distance of the Pt band from the membrane-CCL interface where δ_M is the thickness of the membrane; p_{H_2} is the partial pressure of H_2, p_{O_2} is the partial pressure of O_2; while K_{H_2} and K_{O_2} are the permeabilities of H_2 and O_2 through the membrane respectively.

Finally, at the CCL-gas diffusion layer (GDL) interface, there is zero flux for platinum ion concentration to eliminate any cross-over.

$$\left.\frac{\partial c_{Pt^{2+}}}{\partial x}\right|_{x=L_{CCL}} = 0 \tag{15}$$

The source term in Eq. 10 represents the Pt^{2+} ions produced by the net rate of dissolution, $r_{net,Pt^{2+}}$. After discretization, the source term in each control volume is assumed as S_i and it takes the form:

$$S_i = \sum_{j=1}^{M} \frac{\frac{\pi}{2}\left(d_{i,j}\right)^2 Num_{i,j} r_{net,Pt^{2+}}}{N} \tag{16}$$

In Eq. 16, $Num_{i,j}$ (units of $1/m^3$) refers to the number density or equivalently, the number of particles per unit volume based on a Gaussian particle-size distribution (PSD) extracted experimentally[8] (Fig. S2 of the Supporting Information). Eqs. 17 and 18 are utilized to identify the particle number in each diameter group. As seen in Eq. 18, N_1 is assigned as a scaling factor to align the initial PSD with the starting platinum loading present in the pristine sample (considered as m_{Pt} = 0.4 mg/cm^2 in this work). Furthermore, we denote $\hat{a}$ as the active interfacial area (units of 1/m) which can be determined based on the mass loading (m_{Pt}), the thickness of the CCL (L_{CCL}), and the initial electrochemical active area (ECA) (assumed to be 55 m^2/g) as shown in Eq. 19. It is clear that the ratio of active interfacial area to the geometric surface area (GSA) (expression of GSA is shown in Eq. 20) is a constant during the cycling process and is cognizant of the catalyst utilization. The same has been represented mathematically in Eq. 21. Once, the geometric surface area is obtained at each time step, the active interfacial area can be computed and fed as an input to the pseudo-pore-scale electrochemical performance model.

$$Num_{i,j} = \frac{N_1}{\sigma\sqrt{2\pi}} e^{\left\{-\frac{(d-\mu)^2}{2\sigma^2}\right\}} \tag{17}$$

$$N_1 = \frac{m_{Pt}}{L_{CCL}\rho_{Pt}\sum_{i=1,j=1}^{N,M}\frac{Num_{i,j}}{N_1}\left(\frac{\pi d_{i,j}^3}{12}\right)} \tag{18}$$

$$\hat{a}(t) = \frac{m_{Pt} \times ECA(t)}{L_{CCL}} \tag{19}$$

$$GSA(t) = \sum_{i=1,j=1}^{N,M} Num_{i,j}\left(\frac{\pi d_{i,j}^2}{2}\right) \tag{20}$$

$$\xi = \frac{\hat{a}(0)}{GSA(0)} = \frac{\hat{a}(t)}{GSA(t)} \tag{21}$$

The initial and the remaining Pt mass (or, equivalently loading) after the end of cycling can be calculated by Eqs. (22-24):

$$m_{Pt}(t) = \rho_{Pt}\sum_{i=1,j=1}^{N,M} Num_{i,j}\left(\frac{\pi d_{i,j}^3}{12}\right)L_{CCL} \tag{22}$$

$$m_{Pt}(0) = \rho_{Pt}\sum_{i=1,j=1}^{N,M} Num_{i,j,0}\left(\frac{\pi d_{i,j,0}^3}{12}\right)L_{CCL} \tag{23}$$

$$\Delta m_{Pt,loss} = m_{Pt}(0) - m_{Pt}(t) \tag{24}$$

The active interfacial area losses owing to the Pt mass loss and Ostwald Ripening are computed as per:

$$\Delta\hat{a}_{loss} = \hat{a}(0) \times \frac{\Delta m_{Pt,loss}}{m_{Pt}(0)} \tag{25}$$

$$\Delta\hat{a}_{coarsening} = \left(\hat{a}(0) - \hat{a}(t)\right) - \Delta\hat{a}_{loss} \tag{26}$$

$$\Delta_{loss} = \frac{\Delta\hat{a}_{loss}}{\Delta\hat{a}_{total}} \tag{27}$$

$$\Delta_{coarsening} = \frac{\Delta\hat{a}_{coarsening}}{\Delta\hat{a}_{total}} \tag{28}$$

$$\Delta\hat{a}_{total} = \xi \sum_{i=1,j=1}^{N,M} \left(Num_{i,j}\left(\frac{\pi d_{i,j}^2}{2}\right)\right) - \left(Num_{i,j,0}\left(\frac{\pi d_{i,j,0}^2}{2}\right)\right) \tag{29}$$

It is worth mentioning that Eqs. 25, 26, and 29 can be expressed both in terms of $\hat{a}$ or ECA based on the relationship shown in Eq. 19. The first-order ordinary differential equations (Eqs. 8-9) are discretized and solved using a Euler-explicit method. The initial value of coverage is assumed to be small (of the order of 10^{-5}). The initial platinum concentration is considered zero throughout the domain. Eq. 10 is discretized using an Implicit-Euler scheme for the temporal term and a Central Differencing scheme for the spatial term. The solution of this coupled system of equations yields the magnitude of the final active interfacial area which then serves as an input to the electrochemical performance model described next.

In the context of a numerical strategy concerning particle instability, we take into consideration a limiting or cut-off diameter (d_{lim}), the magnitude of which is 0.99 nm[47]. Essentially when the particle diameter reaches the cut-off limit, the diameter bins are clipped from the particle size distribution as per Eq. 30. The net effect in the rate of dissolution is depicted in Eq. 31:

$$Num_{i,j}\Big|_{d_{i,j}\to d_{\lim}} = 0 \tag{30}$$

$$\begin{aligned} \text{if } d_{i,j} \in \left[d_{\lim}, d_{\lim}+0.01\right) \Rightarrow r_{net,Pt^{2+}} = \Psi r_{net,Pt^{2+}},\ \Psi = 0.5 \\ \text{if } d_{i,j} < d_{\lim} \Rightarrow r_{net,Pt^{2+}} = 0 \end{aligned} \tag{31}$$

The relevant values of all the parameters have been documented in the Supporting Information.

(ii) Reactive transport model:

The performance model of the CCL solves the multiple physico-chemical transport mechanisms in a volume-averaged sense as enumerated in Goswami et al.[50] The assumptions include steady-state operation of the fuel cell under isothermal conditions. In addition, the model is approximated as a single-phase such that the byproduct water is existent only in the gaseous phase. The swelling effect of the ionomer film upon water uptake is also neglected in this work. The relevant governing equations and boundary conditions pertaining to the reactive transport model along with the empirical correlations for bulk ionomer conductivity, Henry's constant, oxygen diffusivity through the ionomer and water content are presented in the Supporting Information (section S5).

The active interfacial area, $\hat{a}$ (Eqs. 19-21) influences the reaction current density which appears as a volumetric source term, j in the governing equations. Due to the sluggish response of the oxygen-reduction reaction, the reaction current density follows Tafel kinetics and can be expressed as:

$$j = -\hat{a} i_o \left(\frac{c_{\mathrm{O_2}}^{reaction\ site}}{c_{\mathrm{O_2}, ref}} \right) \exp\left(\frac{-\alpha_c F}{RT} \eta \right) \tag{32}$$

The overpotential, η can then be written as:

$$\eta = \phi_s - \phi_e - U \tag{33}$$

where, U is the reversible open-circuit potential at the fuel-cell operating temperature and pressure.

In terms of the mass transport resistances, the coupled modes can be deconvoluted and identified as: (i) local oxygen resistance through the ionomer thin film (Eq. 34), (ii) oxygen resistance as it pervades through the tortuous pathway of the pore network (Eq. 35), and (iii) oxygen resistance through the gas diffusion layer (Eq. 36). The combined effect results in a limiting current density scenario (Eq. 37) where there is an absence of reactant reaching the catalytic sites. This severity manifests through the concentration overpotential that further exacerbates the polarization losses as observed in Eq. 38.

$$R_{ionomer} = \frac{\hat{t} \times H_{O_2}}{f_{roughness} D_{O_2}^{ionomer} RT} \tag{34}$$

$$R_{pore} = \frac{c_{O_2}\big|_{x=L_{CCL}} - c_{O_2}\big|_{x=0}}{\left(\frac{I}{4F}\right)} \tag{35}$$

$$R_{GDL} = \frac{L_{GDL}}{\left(D_{O_2} \frac{\varepsilon}{\tau}\right)_{GDL}} \tag{36}$$

$$i_{\lim} = \frac{c_{O_2,\, inlet} \times 4F}{R_{ionomer} + R_{pore} + R_{GDL}} \tag{37}$$

$$\eta_{concentration} = \left(\frac{RT}{4F}\right) \ln\left(\frac{i_{\lim}}{i_{\lim} - I}\right) \tag{38}$$

In Eq. 34, $f_{roughness}$ represents the roughness factor[51] which is a product of the electrochemical active area - ECA (m^2/g) and the platinum mass loading - m_{Pt} (mg/cm^2) and is essentially non-dimensional in nature. It can also be expressed as an effective active interfacial area per unit area of the membrane-electrode assembly (MEA) as per Eq. 39 and had been previously presented by Nonoyama et al.[52]

$$f_{roughness} = ECA \times m_{Pt} = \hat{a} \times L_{CCL} \tag{39}$$

Eqs. 34 and 39 further illustrate the inverse scaling of the local transport resistance through the ionomer with the active interfacial area. This aspect bears significance as the coupling between the two models (degradation model with the reactive transport model) is accomplished through the change in active interfacial area and the local oxygen transport resistance which are a function of the transient cycling process.

3. Results and discussion:

Herein, we have highlighted the degradation-induced performance loss in Polymer Electrolyte Fuel Cell catalyst layers through a physics-based mechanistic analysis. The features of an end-of-life (EOL) electrode have been probed to evaluate distinct signatures engendering from catalyst aging. The influence of operating variables like temperature, relative humidity, ionomer volume fraction, mean particle size, etc. on the potentiostatic (potential-cycling) degradation has been reported. Further, deconstruction of the change in the active area through competing mechanisms in the form of coarsening and dissolution-induced loss have been computed and analyzed in detail. A grid independence exercise has also been performed to ascertain that the numerical code is not dependent on the mesh size adopted as shown in the Supplementary Information (Fig.

S3). A grid size of (25 x 100) has been adopted for all simulations. Also, the thermo-kinetic parameters have been extracted by fitting to an experimental cyclic voltammetry (CV) profile as has been highlighted in Fig. S4(a) of the Supporting Information.

3.1 Degradation stressors reveal instability signature:

For the subsequent discussion, we steer our attention to the characteristics of an EOL electrode after it has been subjected to a degradation sequence. The conditions include a triangular wave potential sweep from 0.4-1.0 V under H_2-Air conditions for 10,000 cycles at moderate temperature (80°C) and moderate relative humidity (60% RH). The ionomer volume fraction is 0.2 and the mean particle size is considered as 2.8 nm. Fig. 2 shows the general features of degradation-induced change in the catalyst layer environment. It is worth mentioning that the degradation tends to be non-uniform both in the transport direction and diameter space; and hence, the local effects need to be appropriately expounded. In this regard, we report the percentage change in diameter and its relationship with the initial diameter and location within the catalyst layer at the end-of-life (after 10,000 cycles) in Fig. 2(a). A positive value of percentage change in the diameter leads to growth or coarsening zone while on the other hand, a negative value of percentage change in the diameter leads to a shrinking zone. The contour map reveals that the maximum change that occurs in a particle distribution is through a shrinking mechanism (~ 60% maximum negative change) rather than a coarsening mechanism (~ 5% maximum positive change). Also, with respect to the shrinking zone, the highest (more negative) change is seen in a zone that has an initial diameter ranging from 2 - 2.6 nm. Below this initial diameter range, the percentage change, however, is lowered owing to the extreme instability of the particles, which leads to dissolution to a critical diameter within a much shorter span of cycling time. Analogously, the final diameter at the end of cycling has been depicted in Fig. 2(b).

It must be noted that a diameter range from 1.5 nm (the lowest value in the particle size distribution) till 2.6 nm almost reaches a final value of 0.99 nm at the end of life. We refer to this limit as the critical or the cut-off diameter zone where the particles are fully dissolved with the net effect resulting in zero rates of dissolution or the diameter bins being truncated from the PSD as already mentioned in the mathematical description section. Based on Fig. 2(a), we identify specific regime maps in Figs. 2(c) revealing the demarcation into coarsening and shrinking regions with the zero-percentage change dictating the boundary transition. It is seen that the shrinking zone spans a greater area towards the membrane-CCL interface which can be attributed to the existence of a concentration gradient that results in platinum band formation within the membrane. Based on the information extracted from Figs. 2(b) and (c), we reveal in Fig. 2(d) that the shrinking zone can be further distinguished into a stable regime - for particle bins where the magnitude of final diameter is greater than the cut-off value, or, in other words, the limiting diameter and an unstable regime - where the final diameter reaches the limiting value. It is notable to mention here that the stability signatures accrued as a result of the long-term cycling would be highly dependent on the set of operating conditions. In Fig. 2(e), a comparative assessment of the relevant fluxes (rate of particle dissolution vs rate of particle oxidation vs the diffusive flux at the membrane-CCL interface) has been carried out for the first period of the corresponding waveform pertaining to the smallest diameter of the particle distribution. It is seen that the rate of oxidation is the dominant flux mechanism that dictates the degradation and supersedes the least dominant mode, that is, the Pt^{2+} diffusive flux (Eq. 40) by 3 orders of magnitude. Both the net Pt dissolution rate and the Pt^{2+} diffusive flux exhibit a Nernstian behavior and reach their peaks at the same time as the upper potential limit. Furthermore, the asymmetry in the anodic and cathodic front in the net Pt oxidation rate stems

from the difference in the transfer coefficients corresponding to the two regions (0.5 and 0.35 for the anodic and cathodic halves respectively).

$$\mathrm{Pt}^{2+}\text{diffusive flux} = -\varepsilon_{ionomer}^{1.5} D_{Pt^{2+}}^{ionomer} \left.\frac{\partial c_{Pt^{2+}}}{\partial x}\right|_{x=0} \tag{40}$$

The interplay of operating conditions in the form of relative humidity and temperature on the change in ECA has been highlighted in the contour map in Fig. 3(a). From the phase map, it is noticed that the severity of catalyst degradation is pronounced at high temperature and fully humidified conditions. The implication of relative humidity on the degradation and performance has been analyzed in detail in Figs. 3(b-d). Three values of relative humidity have been considered for the analysis - 20%, 60%, and 100% with other significant parameters being $T = 80°C,\ \varepsilon_{ionomer} = 0.20,\ \mu = 2.8\ nm$. To understand the influence of relative humidity on the electrochemical response as shown in Fig. 3(b), the difference originating in a pristine electrode at 20% and 100% RH (red and blue solid curves respectively) has to be elucidated in a mechanistic sense. In the ohmic regime, the enhancement in bulk ionomer conductivity with the increase in water content as a result of better humidification leads to lower overpotential at 100% RH. However, beyond the ohmic regime, a lower mole fraction of gaseous oxygen reactant indicates that the limiting current density or the mass transport tail is approached earlier at 100% RH. The average difference between a pristine and a cycled electrode (difference between the solid and dashed curves for the corresponding color) is around 19.7 mV at 100% RH while at 20% RH, the difference is 1.53 mV thereby indicating severe degradation when the humidification content is higher in the catalyst layer. The sensitivity of the local transport resistance to relative humidity has been shown in Fig. 3(c) at three different stages of the degradation sequence, namely. pristine and after the completion of 5000 and 10,000 cycles. For

a pristine electrode, the resistance decreases with the increase in the magnitude of relative humidity. This behavior can be attributed to the enhancement in the diffusivity of oxygen through the ionomer with increased hydration or relative humidity in the catalyst layer. However, once the effects of degradation set in, the sensitivity scaling gets reversed due to the inverse dependence of the local transport resistance with the ECA as seen in Eq. 34. In fact, due to the larger drop in the ECA at the highest relative humidity, the local transport resistance is amplified by ~91% at 100% RH at the end of 10,000 cycles compared to the pristine case. In Fig. 3(d), we present a non-dimensional onset time (Eq. 41), t_{onset} as a function of the initial diameter bin at varying magnitudes of relative humidity. It is essentially a transient descriptor that represents the cycle time required for a particular diameter bin to reach the limiting diameter value, 0.99 nm. In a physical sense, it implies the instant when the particles transition from Pt to Pt^{2+}, or in other words, a solution mode. The onset time is formulated as a power-law fit to the initial diameter bins normalized by the mean value of the relevant particle size distribution and the concomitant operating variable to develop scaling relations. Throughout this work, we refer to the onset time determined for particles residing in the vicinity of the membrane-CCL interface (shrinking zone as per Fig. 2(c)). The relevant expression that connects the onset time with the normalized initial diameter bins and relative humidity is highlighted in Eq. 42. It is interesting to note that as RH is progressively increased, a greater number of diameter groups undergo complete dissolution and approach the limiting diameter.

$$t_{onset} = \frac{t_{d_{initial} \to d_{\lim}}}{t_{final}} \tag{41}$$

$$t_{onset}\left(d, RH\right) = 0.9544\left(\frac{d}{\mu}\right)^{8.5476} RH^{-1.7637},\ R^2 = 0.995 \tag{42}$$

A similar analysis has been performed to delineate the implication of temperature on the degradation and performance as seen in Figs. 3(e-g). Three values of temperature have been considered for the analysis - 60℃, 80℃, and 90℃ with other significant parameters being $RH = 100\%,\ \varepsilon_{ionomer} = 0.20,\ \mu = 2.8\ nm$. To discern the difference in the response for a pristine electrode at 60℃ and 90℃ (red and blue solid curves respectively), we report the change in the relevant electrochemical performance as shown in Fig. 3(e) and accordingly segregate the dependence of the kinetic and the ohmic regimes with the temperature. Firstly, the faster tendency of reaction rates at high temperatures indicates that the kinetic overpotential at 90℃ is lower. Further, the decrease in water activity (Eq. S17 of the Supporting Information) with the increase in temperature means that the bulk ionomer conductivity (Eq. S13 of the Supporting Information) is lowered leading to higher overpotential in the ohmic regime for 90℃ in comparison to that at 60℃. The decrease in reaction current density and increase in local oxygen transport resistance are responsible for the difference in performance between the pristine and the cycled electrode (solid and dashed lines respectively). The corresponding difference is around 28.1 mV at 90℃ while at 60℃, the same difference is 8.7 mV further cementing the fact that degradation is accelerated at higher temperatures. In Fig. 3(f), the relationship of the local transport resistance with respect to temperature is represented in an analogous manner to Fig. 3(c). Due to the exponential dependence of oxygen diffusivity (penetrating through the ionomer domain) with temperature, the local resistance decreases for a pristine case. However, at 5000 and 10,000 cycles, the drop in ECA induces a reversal in the previous trend that impacts the temperature sensitivity. Due to the decay in electrochemical active area with cycling and the inverse dependence of the local oxygen transport resistance with the same, it can be now observed that the resistance increases with temperature thereby originating mass-transport

limitations. In other words, the sensitivity with respect to the active area is relatively dominant when compared to that to temperature. In Fig. 3(g), we present the non-dimensional onset time, t_{onset} as a function of the normalized initial diameter bins at varying magnitudes of temperature; the relevant scaling relation is expressed in Eq. 43. If the temperature is raised incrementally and a fixed diameter bin is considered, the onset time reduces remarkably which is also quite evident from the high negative exponent (- 15.334) over the dimensionless temperature group in the scaling relation.

$$t_{onset}\left(d,T\right)=44.355\left(\frac{d}{\mu}\right)^{7.667}\left(\frac{T}{T_o}\right)^{-15.334},\ R^2=0.997 \tag{43}$$

We identify that the dissolved Pt mass can either undergo coarsening or escape the catalyst layer system leading to a loss in the catalyst inventory. Accordingly, the change in ECA occurs through either a loss mechanism (Eq. 27) or a coarsening mechanism (Eq. 28). The consequent dependence on temperature and relative humidity is probed through four scenarios – (i) low RH, low temperature $\left(RH=20\%,\ T=60°C\right)$, (ii) low RH, high temperature $\left(RH=20\%,\ T=90°C\right)$, (iii) high RH, low temperature $\left(RH=100\%,\ T=60°C\right)$, and (iv) high RH, high temperature $\left(RH=100\%,\ T=90°C\right)$as exhibited in the bar diagram in Fig. 3(h). It is clear that the dominant mechanism in all the cases is the inventory loss phenomenon which gets most aggravated in the zone of severity, i.e., high temperature and fully humidified conditions, and can be primarily ascribed to the promotion of dissolution rates for catalyst particles. A salient aspect to note here is that the contribution through the coarsening mechanism escalates under low humidification conditions. This is due to the degradation being majorly dictated by the increased tendency of backward reaction, i.e., the redeposition reaction shown in Eq. 1.

3.2 Microstructural attributes to performance-degradation interactions:

The ionomer phase distributed in the catalyst layer serves as a medium through which the Pt^{2+} ions can diffuse to finally re-precipitate as a band within the membrane. As such, the influence of this significant microstructural metric in the form of ionomer volume fraction, $\varepsilon_{ionomer} = 0.10, 0.15, 0.20$ on the coupled degradation-performance characteristics has been reported in Fig. 4. The analysis has been carried out in the most exacerbated zone corresponding to Fig. 3(a), in other words, the region of full humidification and high temperature $\left(RH = 100\%,\ T = 90°C\right)$ while keeping the initial area the same for all three cases (= 55 m^2/g). The mean particle size is considered 2.8 nm. It is interesting to observe that the decay in the electrochemical active area after a duration of 10,000 cycles (~ 40% of the initial ECA) is not sensitive to the change in the ionomer volume fraction which is quite evident from Fig. 4(a). The reason for this behavior stems from the suppressed contribution from the Pt^{2+} diffusive flux offered by the ionomer as already discussed in Fig. 2(e). As a result, the average difference in the electrochemical performance between a pristine and cycled electrode (Fig. 4(b)) also remains the same around 28 mV across the two extreme ionomer volume fractions (= 0.10 and 0.20). The severity of concentration overpotential (the term $\left(\frac{i_{\lim}}{i_{\lim} - I}\right)$ in Eq. 38) for the end-of-life electrode is illustrated in Fig. 4(c) to show the interplay between the operating current density (in the mass transport regime) and the ionomer content. The region colored in white is indicative of a non-permissible operating zone wherein limiting current density has been encountered. It is seen that the onset of limiting current ensues earlier at the highest ionomer volume fraction because of the increase in tortuosity of the electrode at the expense of the pore space in addition

to the presence of a bulkier ionomer film. The onset time is shown in Fig. 4(d) which shows an overlap throughout the range considered at all the diameter bins. The small magnitude of the power-law coefficient (0.00062405) in the scaling relation shown in Eq. 44 further justifies the fact that degradation characteristics are independent of the ionomer volume fraction. As far as the contribution to the drop in ECA is concerned, the loss mechanism is the dominant mode with a nominal increase in dissolution-induced loss as seen in Fig. 4(e). Hence, it can be surmised that after the aging landscape is elapsed, the differentiator in the evaluated electrochemical response is solely due to the structural changes (effective microstructural properties are enlisted in Table 1) in the catalyst layer due to the change in the ionomer volume fraction.

$$t_{onset}\left(d,\varepsilon_{ionomer}\right)=0.56016\left(\frac{d}{\mu}\right)^{7.0597}\varepsilon_{ionomer}^{-0.00062405},\ R^2=0.999 \tag{44}$$

Next, we focus on a mechanistic understanding of the influence of another microstructural variable in the form of mean catalyst diameter of the particle size distribution. First of all, it is necessary to construct nanometer sized Pt primary particles to boost the reaction efficacy of the catalyst layer. However, in this context, there exists a tradeoff between performance and degradation that needs further elaboration. The Gibbs-Thomson potential is highest for particle sizes ranging between 2-3 nm and decreases significantly beyond 5 nm[35]. A slight increase in the particle sizes beyond the commonly used 2-3 nm values can enormously promote the stability. However, using large particle sizes beyond a threshold can also drop the initial specific activity and thereby result in below par performance of the fuel cell due to an increase in the kinetic overpotential - the most dominant resistance mode in the thin catalyst layer.

We probe three mean catalyst diameters, $\mu = 2,\ 2.8,\ 3.7$ nm of the particle size distribution (the relevant profiles are plotted in Fig. S2 of the Supporting Information); the resulting degradation-

performance characteristics have been delineated in Fig. 5. The analysis has been performed simulating the most severe conditions $\left(RH = 100\%,\ T = 90°C\right)$ with $\varepsilon_{ionomer} = 0.20$. It must be highlighted here that, in this work, while assessing the effect of mean particle sizes, the starting area for the pristine electrode configuration (= 55 m^2/g) is kept the same for all three cases which suggests that the number density for the distribution with the smallest mean diameter would be the highest. This argument is congruent with the experimentally observed initial ECA which is almost the same for electrodes with mean particle sizes 2.2 nm and 3.5 nm reported in Yu et al.[53] Working with samples with mean particle sizes greater than 10 nm showed infeasible initial fuel cell performance due to extremely low ECA. Once potential cycling is accomplished after the passage of 10,000 cycles, we report the transient evolution of the electrochemical active area in Fig. 5(a). From the figure, it is quite evident that the decay in ECA is highly sensitive to the change in the mean diameter with the drop asymptotically reaching as low as 2% for μ = 2 nm. As a result, there exists a stark difference (~ 123 mV) in the electrochemical performance between a pristine and cycled electrode (Fig. 5(b)) at μ = 2 nm, while the difference in the case of μ = 3.7 nm is less (~ 6.2 mV) due to higher retention of the ECA (~ 81% of the initial value). The severity of concentration overpotential for the end-of-life electrode is illustrated in Fig. 5(c) to show the interrelationship between the operating current density and the mean particle diameter. Towards larger operating current densities and small mean particle sizes, the concentration overpotential further worsens owing to the increment in local oxygen transport resistance as a consequence of the acute degree of catalyst degradation. The accumulation of cumulative instability fronts incurred during the electrode operation at μ = 2 nm is manifested through the significantly low values of onset times as observed in Fig. 5(d). Approaching the limiting diameter in the case of several normalized diameter bins having a magnitude greater

than unity is also a fingerprint of the accelerated impact of the deleterious mechanisms. This is reflected in Fig. 5(e) which shows the absence of coarsening mechanisms and participation of a pure inventory loss-driven degradation mode that contributes to the rapid drop of the valuable electrochemical active area at μ = 2 nm. Therefore, an optimum diameter range consisting of mid-sized particles (3.5 – 5.5 nm) can tend to show remarkable stability and result in a maximum performance with minimum performance decay.

3.3 Interfacial complexations:

The electrocatalysis associated with oxygen reduction reaction (ORR) in fuel cells is a multi-dimensional design space[54,55]. In this context, interfacial engineering is an aspect that plays a pivotal role in tailoring the durability functionality of a catalyst layer. In a recent study by Li et al.[28], the traditional Nafion®-Pt interface was replaced with a block copolymer that could enhance the coverage-dependent kinetics[56] thus alleviating the kinetic losses. The influence of the Pt oxide-oxide interaction energy (ω) on the degradation-performance characteristics is thus reported in Fig. 6. Two values of ω (= $0.8\text{x}10^5$ and $4\text{x}10^5$ J/mol) have been considered for the analysis at $RH = 100\%,\ T = 90°C$ with $\varepsilon_{ionomer} = 0.20,\ \mu = 2$ nm. Fig. 6(a) exhibits the Pt-oxide coverage over the minimum diameter (= 1.5 nm) of the PSD at the membrane-CCL interface for an initial period of 4 cycles of the triangular waveform. We emphasize on the change in chemical potential which leads to the reversible formation of oxide coverage over the bare surface of the catalyst particles (Eq. 2) and drives the forward kinetic rate expression (Eq. 6) as shown in Eq. 45. It is seen that on increasing the value of ω, the chemical potential differential reduces which indicates a lesser propensity of the forward reaction of PtO layer formation. Hence, the oxide coverage at ω = 4 x 10^5 J/mol would be much lesser than the corresponding coverage at ω = 0.8 x 10^5 J/mol. In addition, due to the inverse dependence of Eq. 45 with particle diameter[33], less

fractional coverage is observed at the largest diameter of the distribution when compared to the least diameter of the distribution. This trend is aptly observed in the maximum diameter (6.5 nm) case as seen in Fig. 6(b). The coverage-dependent kinetics highlighted in Figs. 6(a) and (b) have a profound impact on the degradation characteristics as seen in Fig. 6(c) with higher ECA decay observed at the interface with high oxide-oxide interaction energy. This is indicative of the fact that the lower the extent of the oxide monolayer coverage, higher is the propensity of the rate of the particles to proceed towards dissolution. The same effect is manifested in the trend of onset time, t_{onset} as seen in Fig. 6(d) which depicts that the diameter bins tend to quicky get solvated if the interface possesses higher oxide adsorption energy. The loss mechanism still dominates the coarsening mechanism with a slight increase in dissolution induced loss with ω as observed in Fig. 6(e).

$$\Delta\mu_{\mathrm{Pt}\rightarrow\mathrm{PtO}} = \frac{\gamma_{Pt}\Omega_{Pt}}{d_{i,j}} - \frac{\gamma_{PtO}\Omega_{PtO}}{d_{i,j}} - \omega\theta_{i,j} \tag{45}$$

In a nutshell, it can be surmised that the efficacy of the ORR is decreased due to various concurrent deleterious mechanisms at play – dissolution/ reprecipitation of the nano-sized catalyst particles, formation of platinum oxide over the bare surface of the catalyst, and diffusion of platinum ions through the ionomer phase and consequent precipitation in the membrane. These aforementioned phenomena affect the life expectancy of an operating fuel cell and need to be appropriately suppressed. This impediment alters the electrochemical observables through increased overpotential and high oxygen transport resistance at the catalyst-support interface thereby leading to a drop in performance. The degradation-performance characteristics are highly dependent on extrinsic parameters like the type of durability protocols and the effect of scan

rates and dwell rates in addition to microstructural inputs such as the mean and dispersion of the particle size distribution, ionomer volume fraction, etc.

4. Conclusions:

In this work, a scale-bridging mesoscale model has been formulated that couples both the performance and long-term durability of a PEFC catalyst layer. A standard durability test protocol that complies with the potentiostatic conditions is employed to simulate the catalyst aging phenomena. The effect of operating parameters – temperature, relative humidity, ionomer volume fraction, mean particle size, oxide-oxide interaction parameter has been analyzed. In addition, the local behavior of catalyst degradation has been highlighted through coarsening and dissolution zones. Also, dominant mechanisms that lead to the drop in the electrochemical active area have been deconvolved and reported. Following are the key conclusions:

(i) The heterogeneous nature of catalyst-induced degradation arises due to a concentration sink at the membrane and can be quantified through coarsening and shrinking zones. The area spanned by the zones is critically dependent on the operating conditions. The shrinking zone can be further distinguished into stable and unstable regimes on the propensity of the particle bins reaching a cut-off diameter.

(ii) An assessment of the operating fluxes reveals that the degradation is dominated by a particle oxidation/ reduction mechanism. The diffusive flux is dormant and its contribution to the decay in area loss is minimal.

(iii) The severity of degradation is pronounced at high temperatures and fully humidified conditions of the electrode. This in turn leads to exacerbated overpotentials for an end-of-life electrode.

(iv) The local transport resistance adheres to a decreasing trend under high temperature and RH due to the increase in oxygen diffusivity through the ionomer. However, a sensitivity analysis under various stages of cycling highlights its strong inverse dependence on the active interfacial area.

(v) The onset time for a particle diameter to undergo complete dissolution shows a positive power-law correlation with the initial diameter. However, it is anti-correlated as the temperature and relative humidity is progressively increased.

(vi) Decoupling of the change in ECA into inventory loss and coarsening modes depict the tendency of redeposition under low humidification conditions. But, at high temperatures as high as 90°C, particle dissolution gets triggered severely and supersedes other countering mechanisms.

(vii) The decay in ECA is invariant of the change in ionomer volume fraction and so is the onset time and the electrochemical response. The severity of mass transport limitations, in this case, is solely governed by the structural changes in the porous electrode of the catalyst layer.

(viii) A smaller mean particle size encounters a rapid drop in the ECA due to very low onset times thereby leading to high overpotentials. On the other hand, a distribution with a large mean particle size ensures that degradation is suppressed and in turn, delays the approach of limiting current density.

(ix) The larger extent of oxide coverage over the catalyst nanoparticles at low oxide-oxide interaction energy protects against the dominant dissolution mode and accordingly retains a greater proportion of the electrochemical active area.

Acknowledgement: Financial support from National Science Foundation (NSF grants: 1805215 and 1805183) is gratefully acknowledged.

References:

1 Z. Abdin, A. Zafaranloo, A. Rafiee, W. Mérida, W. Lipiński and K. R. Khalilpour, *Renewable and Sustainable Energy Reviews*, 2020, **120**, 109620.

2 D. N. N. Pivovar, B.S., Ruth, M.F., Myers D.J., *ECS Interface*, 2021, **30**, 61–65.

3 Z. P. Cano, D. Banham, S. Ye, A. Hintennach, J. Lu, M. Fowler and Z. Chen, *Nature Energy*, 2018, **3**, 279–289.

4 A. Kongkanand and M. F. Mathias, *Journal of Physical Chemistry Letters*, 2016, **7**, 1127–1137.

5 O. Gröger, H. A. Gasteiger and J.-P. Suchsland, *Journal of The Electrochemical Society*, 2015, **162**, A2605–A2622.

6 M. K. Debe, *Nature*, 2012, **486**, 43–51.

7 P. J. Ferreira, G. J. la O', Y. Shao-Horn, D. Morgan, R. Makharia, S. Kocha and H. A. Gasteiger, *Journal of The Electrochemical Society*, 2006, **152**, A2256.

8 D. J. S. Sandbeck, D. J. S. Sandbeck, M. Inaba, J. Quinson, J. Bucher, A. Zana, M. Arenz, M. Arenz and S. Cherevko, *ACS Applied Materials and Interfaces*, 2020, **12**, 25718–25727.

9 D. Banham and S. Ye, *ACS Energy Letters*, 2017, **2**, 629–638.

10 P. Ren, P. Pei, Y. Li, Z. Wu, D. Chen and S. Huang, *Progress in Energy and Combustion Science*, 2020, **80**, 100859.

11 Ş. Neaţu, F. Neaţu, I. M. Chirica, I. Borbáth, E. Tálas, A. Tompos, S. Somacescu, P. Osiceanu, M. A. Folgado, A. M. Chaparro and M. Florea, *Journal of Materials Chemistry A*, 2021, **9**, 17065–17128.

12 A. P. Soleymani, L. R. Parent and J. Jankovic, *Advanced Functional Materials*, 2022, **32**, 2105188.

13 M. Prokop, M. Drakselova and K. Bouzek, *Current Opinion in Electrochemistry*, 2020, **20**, 20–27.

14 W. Bi and Thomas. F. Fuller, *Journal of The Electrochemical Society*, 2008, **155**, B215.

15 W. Bi, Q. Sun, Y. Deng and T. F. Fuller, *Electrochimica Acta*, 2009, **54**, 1826–1833.

16 W. Bi, G. E. Gray and T. F. Fuller, *Electrochemical and Solid-State Letters*, 2007, **10**, 101–104.

17 J. Zhang, B. A. Litteer, W. Gu, H. Liu and H. A. Gasteiger, *Journal of The Electrochemical Society*, 2007, **154**, B1006.

18 S. Mitsushima, Y. Koizumi, S. Uzuka and K. I. Ota, *Electrochimica Acta*, 2008, **54**, 455–460.

19 M. Matsumoto, T. Miyazaki and H. Imai, *Journal of Physical Chemistry C*, 2011, **115**, 11163–11169.

20 A. Kongkanand and J. M. Ziegelbauer, *Journal of Physical Chemistry C*, 2012, **116**, 3684–3693.

21 D. J. S. Sandbeck, N. M. Secher, F. D. Speck, J. E. Sørensen, J. Kibsgaard, I. Chorkendorff, S. Cherevko and S. Cherevko, *ACS Catalysis*, 2020, **10**, 6281–6290.

22 G. S. Harzer, J. N. Schwämmlein, A. M. Damjanović, S. Ghosh and H. A. Gasteiger, *Journal of The Electrochemical Society*, 2018, **165**, F3118–F3131.

23 A. Kneer, N. Wagner, C. Sadeler, A.-C. Scherzer and D. Gerteisen, *Journal of The Electrochemical Society*, 2018, **165**, F805–F812.

24 A. V. Virkar and Y. Zhou, *Journal of The Electrochemical Society*, 2007, **154**, B540.

25 L. Dubau, J. Durst, F. Maillard, M. Chatenet, J. André and E. Rossinot, *Fuel Cells*, 2012, **12**, 188–198.

26 A. Kneer, J. Jankovic, D. Susac, A. Putz, N. Wagner, M. Sabharwal and M. Secanell, *Journal of The Electrochemical Society*, 2018, **165**, F3241–F3250.

27 P. P. Lopes, D. Li, H. Lv, C. Wang, D. Tripkovic, Y. Zhu, R. Schimmenti, H. Daimon, Y. Kang, J. Snyder, N. Becknell, K. L. More, D. Strmcnik, N. M. Markovic, M. Mavrikakis and V. R. Stamenkovic, *Nature Materials*, 2020, **19**, 1207–1214.

28 Y. Li, T. Van Cleve, R. Sun, R. Gawas, G. Wang, M. Tang, Y. A. Elabd, J. Snyder and K. C. Neyerlin, *ACS Energy Letters*, 2020, **5**, 1726–1731.

29 W. Xu, Z. Wu and S. Tao, *Journal of Materials Chemistry A*, 2016, **4**, 16272–16287.

30 D. Sebastián, C. Alegre, M. E. Gálvez, R. Moliner, M. J. Lázaro, A. S. Aricò and V. Baglio, *Journal of Materials Chemistry A*, 2014, **2**, 13713–13722.

31 T. Fujigaya, S. Hirata and N. Nakashima, *Journal of Materials Chemistry A*, 2014, **2**, 3888–3893.

32 C. Vilela, A. J. D. Silvestre, F. M. L. Figueiredo and C. S. R. Freire, *Journal of Materials Chemistry A*, 2019, **7**, 20045–20074.

33 R. M. Darling and J. P. Meyers, *Journal of The Electrochemical Society*, 2003, **150**, A1523.

34 W. Bi and T. F. Fuller, *Journal of Power Sources*, 2008, **178**, 188–196.

35 E. F. Holby, W. Sheng, Y. Shao-Horn and D. Morgan, *Energy and Environmental Science*, 2009, **2**, 865–871.

36 E. F. Holby and D. Morgan, *Journal of The Electrochemical Society*, 2012, **159**, B578–B591.

37 Y. Li, K. Moriyama, W. Gu, S. Arisetty and C. Y. Wang, *Journal of The Electrochemical Society*, 2015, **162**, F834–F842.

38 P. Schneider, C. Sadeler, A.-C. Scherzer, N. Zamel and D. Gerteisen, *Journal of The Electrochemical Society*, 2019, **166**, F322–F333.

39 Z. Zheng, F. Yang, C. Lin, F. Zhu, S. Shen, G. Wei and J. Zhang, *ACS Applied Materials and Interfaces*, 2020, **12**, 35088–35097.

40 Z. Zheng, F. Yang, C. Lin, F. Zhu, S. Shen, G. Wei and J. Zhang, *Journal of Power Sources*, 2020, **451**, 227729.

41 S. G. Rinaldo, J. Stumper and M. Eikerling, *Journal of Physical Chemistry C*, 2010, **114**, 5773–5785.

42 E. L. Redmond, B. P. Setzler, F. M. Alamgir and T. F. Fuller, *Physical Chemistry Chemical Physics*, 2014, **16**, 5301–5311.

43 H. A. Baroody, G. Jerkiewicz and M. H. Eikerling, *Journal of Chemical Physics*, 2017, **146**, 144102.

44 H. A. Baroody, D. B. Stolar and M. H. Eikerling, *Electrochimica Acta*, 2018, **283**, 1006–1016.

45 M. Prokop, R. Kodym, T. Bystron, M. Paidar and K. Bouzek, *Electrochimica Acta*, 2019, **313**, 352–366.

46 R. Zhang, T. Min, L. Chen, Q. Kang, Y.-L. He and W.-Q. Tao, *Applied Energy*, 2019, **253**, 113590.

47 M. Prokop, R. Kodym, T. Bystron, M. Drakselova, M. Paidar and K. Bouzek, *Electrochimica Acta*, 2020, **333**, 1–17.

48 T. Jahnke, G. A. Futter, A. Baricci, C. Rabissi and A. Casalegno, *Journal of The Electrochemical Society*, 2020, **167**, 013523.

49 C. J. Gommes, *Nanoscale*, 2019, **11**, 7386–7393.

50 N. Goswami, A. N. Mistry, J. B. Grunewald, T. F. Fuller and P. P. Mukherjee, *Journal of The Electrochemical Society*, 2020, **167**, 084519.

51 T. A. Greszler, D. Caulk and P. Sinha, *Journal of The Electrochemical Society*, 2012, **159**, F831–F840.

52 N. Nonoyama, S. Okazaki, A. Z. Weber, Y. Ikogi and T. Yoshida, *Journal of The Electrochemical Society*, 2011, **158**, B416.

53 K. Yu, D. J. Groom, X. Wang, Z. Yang, M. Gummalla, S. C. Ball, D. J. Myers and P. J. Ferreira, *Chemistry of Materials*, 2014, **26**, 5540–5548.

54 D. A. Cullen, K. C. Neyerlin, R. K. Ahluwalia, R. Mukundan, K. L. More, R. L. Borup, A. Z. Weber, D. J. Myers and A. Kusoglu, *Nature Energy*, 2021, **6**, 462–474.

55 C. Y. Ahn, J. E. Park, S. Kim, O. H. Kim, W. Hwang, M. Her, S. Y. Kang, S. Park, O. J. Kwon, H. S. Park, Y. H. Cho and Y. E. Sung, *Chemical Reviews*, 2021, **121**, 15075.

56 N. P. Subramanian, T. A. Greszler, J. Zhang, W. Gu and R. Makharia, *Journal of The Electrochemical Society*, 2012, **159**, B531–B540.

Table 1. Variation of effective microstructural properties with change in ionomer volume fraction $\left(\varepsilon_{ionomer}\right)$

$\varepsilon_{ionomer}$	Effective ionomer conductivity $\left(\kappa^{eff}\right)$	Tortuosity $\left(\tau\right)$	Thickness of the ionomer film $\left(\hat{t}\right)$ (nm)
0.1	0.008022341	1.355719333	4.38351×10^{-9}
0.15	0.019387233	1.453786333	6.57526×10^{-9}
0.20	0.03660639	1.572871667	$8.77\text{E} \times 10^{-9}$

Figure	*Caption*
1	Schematic showing (a) Coarsening of particles due to electrochemical Ostwald ripening (b) Reversible formation/ removal of platinum oxide over the surface of platinum particles, and (c) Dissolution and diffusion of the platinum particles through the ionomer phase in the catalyst layer followed by re-precipitation within the membrane.
2	Probing the general features of potential-cycling induced degradation under moderate temperature and moderate relative humidity: (a) Percentage change in particle diameter at the end-of-life (EOL) stage highlights the heterogeneous nature of catalyst degradation, (b) Final diameter at the EOL stage is an indicator of stability as few particles undergo complete dissolution to reach a critical limiting diameter, (c) Regime map demarcating the percentage change in diameter for the cycled electrode into coarsening and shrinking zones, (d) the shrinking zone from (c) can be further decoupled into unstable and stable regions based on a cutoff being the limiting final diameter from (b), (e) Comparison of fluxes to assess the dominance of relevant mechanisms – this fingerprint is for the initial transient period of the waveform. Conditions include a triangular wave potential cycling from 0.6-1.0 V for 10,000 cycles under H_2-Air condition at $T = 80^{\circ}C,\ RH = 60\%,\ \varepsilon_{ionomer} = 0.20,\ \mu = 2.8\ nm$.
3	Interplay of relative humidity and temperature on potential-cycling induced degradation: (a) Change in ECA as a function of RH and temperature, (b) Electrochemical response for a pristine and cycled electrode at two extreme RH, (c) Sensitivity of local transport resistance with RH at various stages of cycling, (d) Dimensionless onset time and its dependence with normalized initial diameter bins at varying RH, (b-d) are at a fixed temperature of 80°C, (e) Electrochemical response for a pristine and cycled electrode at two extreme temperatures, (f) Sensitivity of local transport resistance with temperature at various stages of cycling, (g) Dimensionless onset time and its dependence with normalized initial diameter bins at varying temperatures, (e-g) are at a fixed relative humidity of 100%, (h) Decoupling into loss and coarsening mechanisms that contribute to ECA change is assessed through four scenarios – (i) low RH, low temperature $\left(RH = 20\%,\ T = 60°C\right)$, (ii) low RH, high temperature $\left(RH = 20\%,\ T = 90°C\right)$, (iii) high RH, low temperature $\left(RH = 100\%,\ T = 60°C\right)$, and (iv) high RH, high temperature $\left(RH = 100\%,\ T = 90°C\right)$. Conditions include a triangular wave potential cycling from 0.6-1.0 V for 10,000 cycles under H_2-Air condition at $\varepsilon_{ionomer} = 0.20,\ \mu = 2.8\ nm$.
4	Influence of ionomer volume fraction on potential-cycling induced degradation at high temperature and fully humidified conditions: (a) Transient evolution of ECA, (b) Electrochemical response for a pristine and cycled electrode at two extreme ionomer volume fractions (0.10 and 0.20), (c)

	Severity of mass transport overpotential and its interplay with operating current density and varying ionomer volume fractions, (d) Dimensionless onset time and its dependence with normalized initial diameter bins at varying ionomer volume fractions, (e) Decoupling into loss and coarsening mechanisms that contribute to ECA change and its dependence on ionomer volume fractions. Conditions include a triangular wave potential cycling from 0.6-1.0 V for 10,000 cycles under H_2-Air condition at $T = 90^{\circ}C,\ RH = 100\%,\ \mu = 2.8\ nm$.
5	Influence of mean particle size on potential-cycling induced degradation at high temperature and fully humidified conditions: (a) Transient evolution of ECA, (b) Electrochemical response for a pristine and cycled electrode at two extreme mean particle sizes (2 nm and 3.7 nm), (c) Severity of mass transport overpotential and its interplay with operating current density and varying mean particle sizes, (d) Dimensionless onset time and its dependence with normalized initial diameter bins at varying mean particle sizes, (e) Decoupling into loss and coarsening mechanisms that contribute to ECA change and its dependence on mean particle sizes. Conditions include a triangular wave potential cycling from 0.6-1.0 V for 10,000 cycles under H_2-Air condition at $T = 90^{\circ}C,\ RH = 100\%,\ \varepsilon_{ionomer} = 0.2$.
6	Influence of platinum oxide-oxide interaction energy on potential-cycling induced degradation at high temperature and fully humidified conditions: Transient evolution of the oxide coverage for the initial four waveforms of the protocol have been shown for (a) minimum diameter and (b) maximum diameter of the distribution; (c) Electrochemical active area decay and (d) Dimensionless onset time and its dependence with normalized initial diameter bins at the two values of platinum oxide-oxide interaction energy, (e) Decoupling into loss and coarsening mechanisms that contribute to ECA change and its dependence on platinum oxide-oxide interaction energy. Conditions include a triangular wave potential cycling from 0.6-1.0 V for 10,000 cycles under H_2-Air condition at $T = 90^{\circ}C,\ RH = 100\%,\ \varepsilon_{ionomer} = 0.2,\ \mu = 2.8\ nm$.

List of figures:

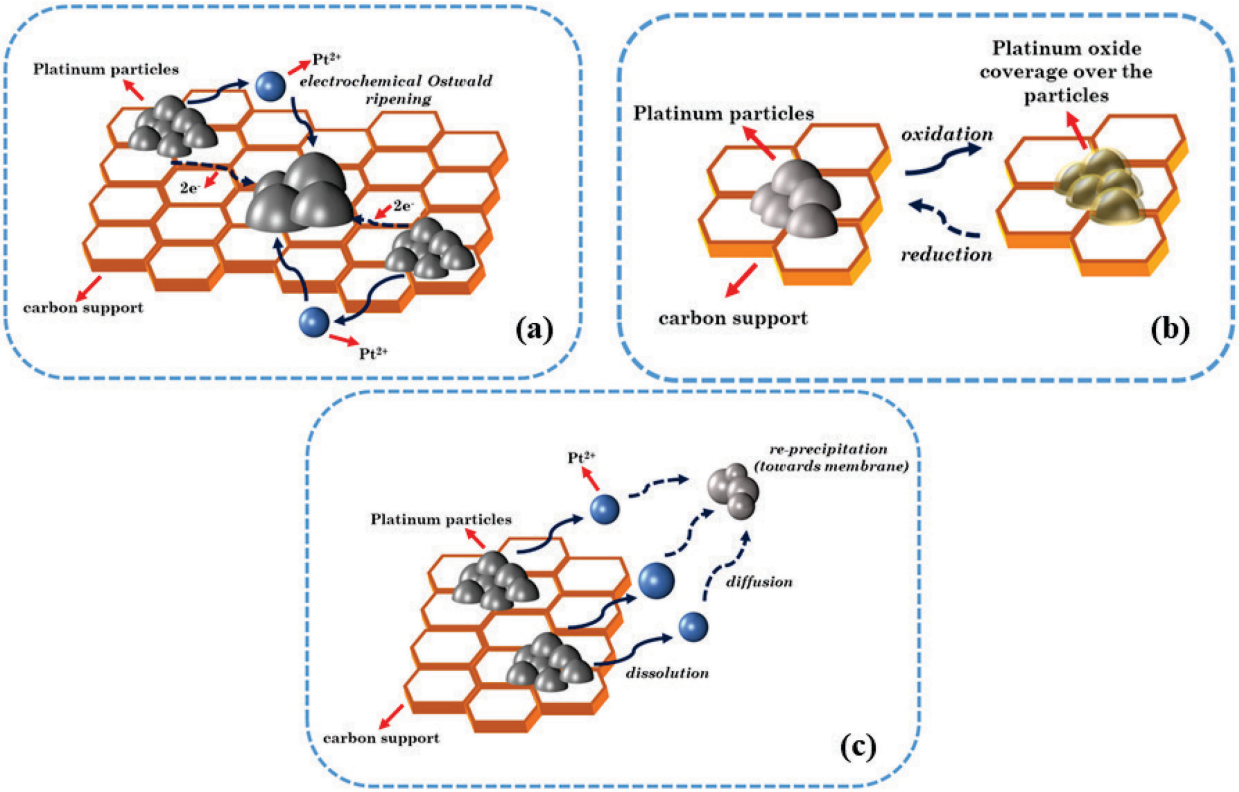

Fig. 1. Schematic showing (a) Coarsening of particles due to electrochemical Ostwald ripening (b) Reversible formation/ removal of platinum oxide over the surface of platinum particles, and (c) Dissolution and diffusion of the platinum particles through the ionomer phase in the catalyst layer followed by re-precipitation within the membrane.

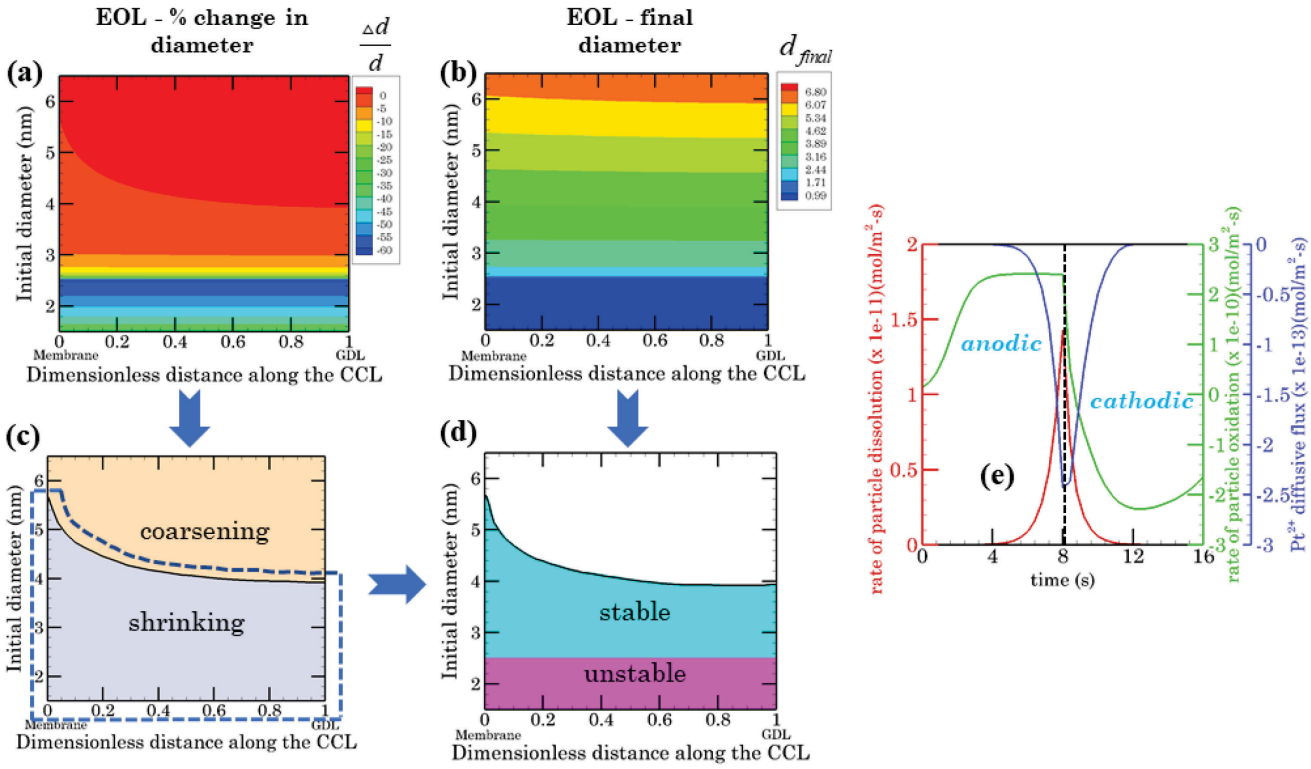

Fig. 2. Probing the general features of potential-cycling induced degradation under moderate temperature and moderate relative humidity: (a) Percentage change in particle diameter at the end-of-life (EOL) stage highlights the heterogeneous nature of catalyst degradation, (b) Final diameter at the EOL stage is an indicator of stability as few particles undergo complete dissolution to reach a critical limiting diameter, (c) Regime map demarcating the percentage change in diameter for the cycled electrode into coarsening and shrinking zones, (d) the shrinking zone from (c) can be further decoupled into unstable and stable regions based on a cutoff being the limiting final diameter from (b), (e) Comparison of fluxes to assess the dominance of relevant mechanisms – this fingerprint is for the initial transient period of the waveform. Conditions include a triangular wave potential cycling from 0.6-1.0 V for 10,000 cycles under H_2-Air condition at $T = 80^{\circ}C$, $RH = 60\%$, $\varepsilon_{ionomer} = 0.20$, $\mu = 2.8\ nm$.

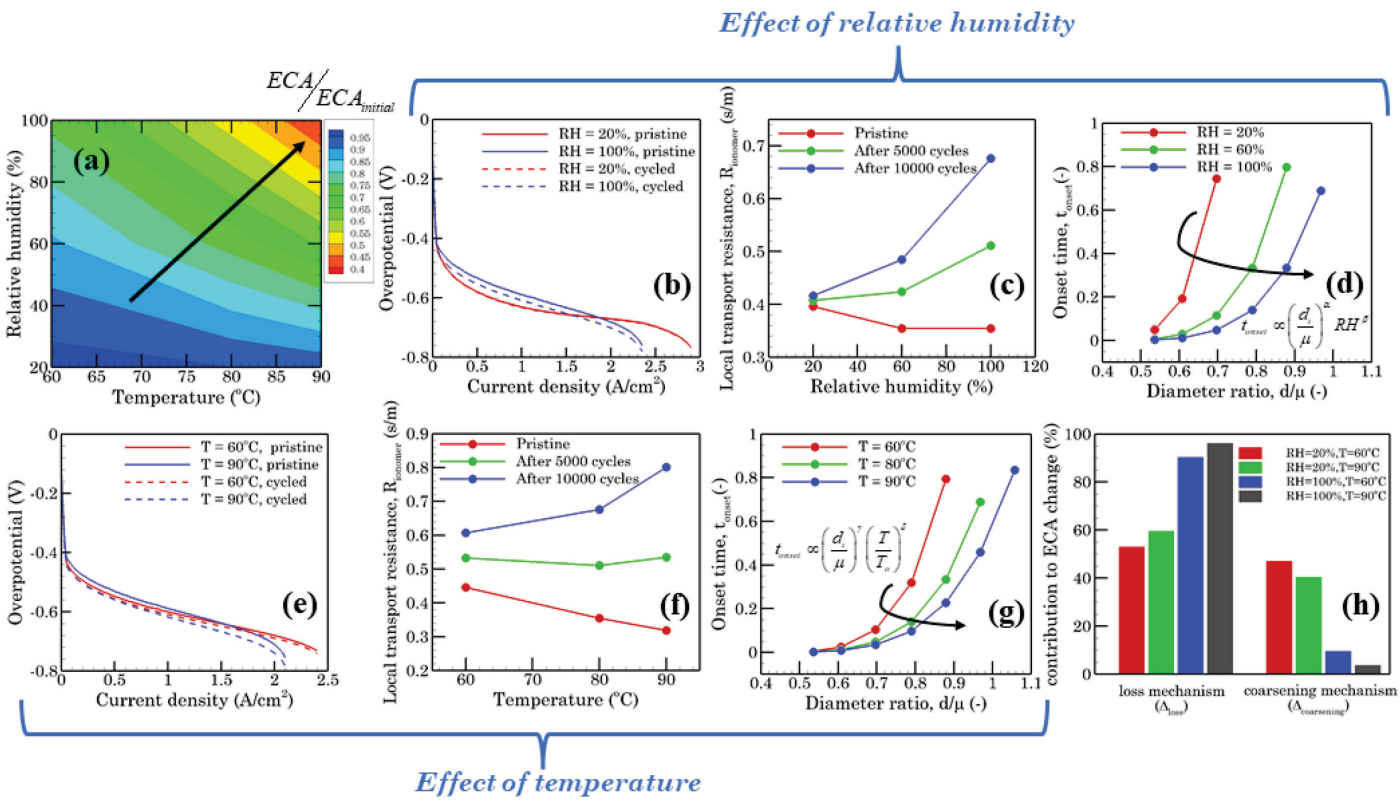

Fig. 3. Interplay of relative humidity and temperature on potential-cycling induced degradation: (a) Change in ECA as a function of RH and temperature, (b) Electrochemical response for a pristine and cycled electrode at two extreme RH, (c) Sensitivity of local transport resistance with RH at various stages of cycling, (d) Dimensionless onset time and its dependence with normalized initial diameter bins at varying RH, (b-d) are at a fixed temperature of 80°C, (e) Electrochemical response for a pristine and cycled electrode at two extreme temperatures, (f) Sensitivity of local transport resistance with temperature at various stages of cycling, (g) Dimensionless onset time and its dependence with normalized initial diameter bins at varying temperatures, (e-g) are at a fixed relative humidity of 100%, (h) Decoupling into loss and coarsening mechanisms that contribute to ECA change is assessed through four scenarios – (i) low RH, low temperature $\left(RH = 20\%,\ T = 60°C\right)$, (ii) low RH, high temperature $\left(RH = 20\%,\ T = 90°C\right)$, (iii) high RH, low temperature $\left(RH = 100\%,\ T = 60°C\right)$, and (iv) high RH, high temperature $\left(RH = 100\%,\ T = 90°C\right)$. Conditions include a triangular wave potential cycling from 0.6-1.0 V for 10,000 cycles under H_2-Air condition at $\varepsilon_{ionomer} = 0.20,\ \mu = 2.8\ nm$.

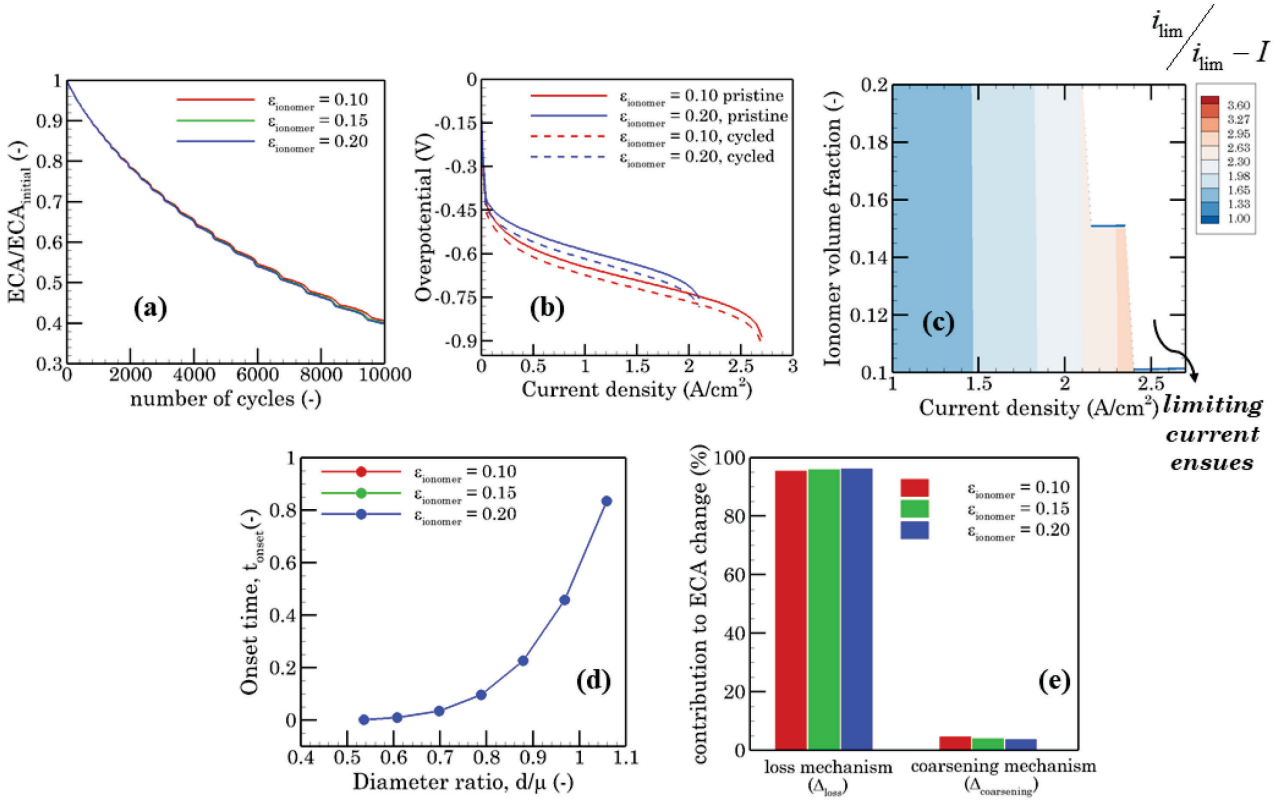

Fig. 4. Influence of ionomer volume fraction on potential-cycling induced degradation at high temperature and fully humidified conditions: (a) Transient evolution of ECA, (b) Electrochemical response for a pristine and cycled electrode at two extreme ionomer volume fractions (0.10 and 0.20), (c) Severity of mass transport overpotential and its interplay with operating current density and varying ionomer volume fractions, (d) Dimensionless onset time and its dependence with normalized initial diameter bins at varying ionomer volume fractions, (e) Decoupling into loss and coarsening mechanisms that contribute to ECA change and its dependence on ionomer volume fractions. Conditions include a triangular wave potential cycling from 0.6-1.0 V for 10,000 cycles under H_2-Air condition at $T = 90^{\circ}C$, $RH = 100\%$, $\mu = 2.8\ nm$.

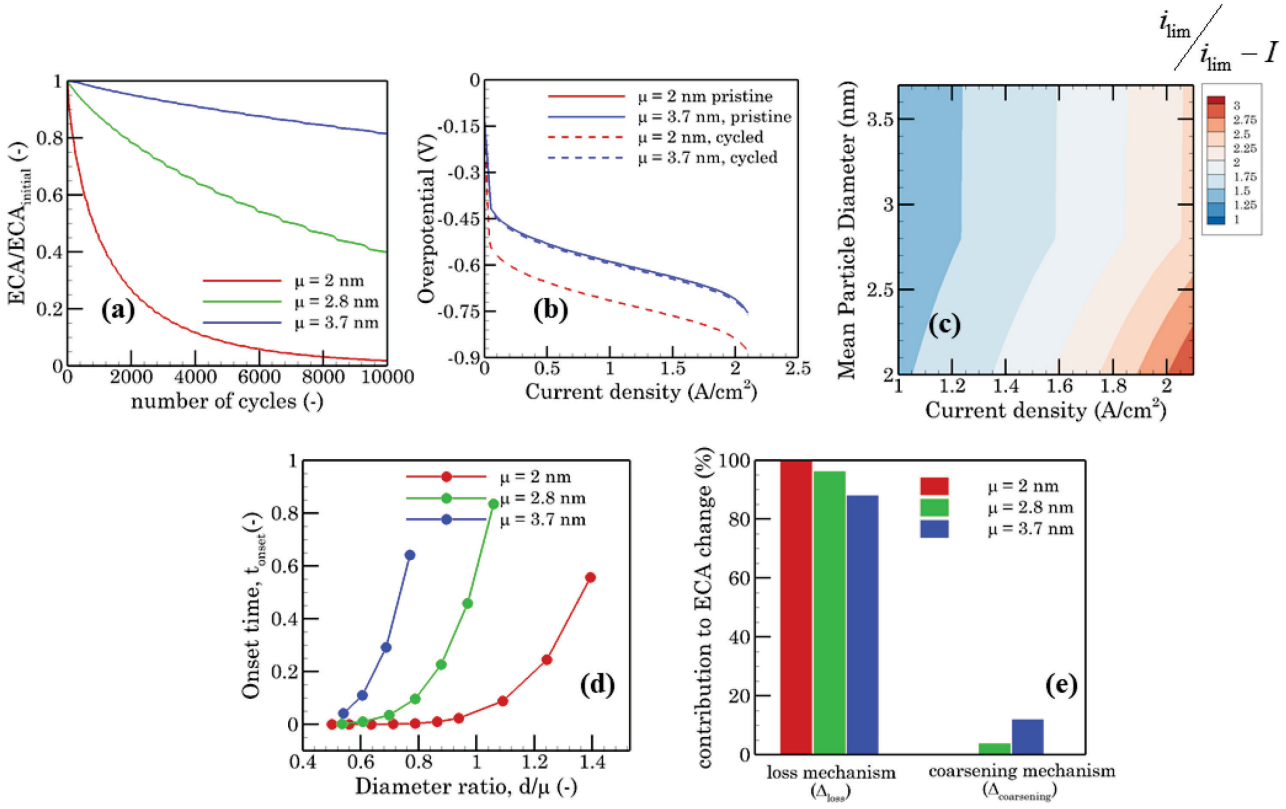

Fig. 5. Influence of mean particle size on potential-cycling induced degradation at high temperature and fully humidified conditions: (a) Transient evolution of ECA, (b) Electrochemical response for a pristine and cycled electrode at two extreme mean particle sizes (2 nm and 3.7 nm), (c) Severity of mass transport overpotential and its interplay with operating current density and varying mean particle sizes, (d) Dimensionless onset time and its dependence with normalized initial diameter bins at varying mean particle sizes, (e) Decoupling into loss and coarsening mechanisms that contribute to ECA change and its dependence on mean particle sizes. Conditions include a triangular wave potential cycling from 0.6-1.0 V for 10,000 cycles under H_2-Air condition at $T = 90^{\circ}C$, $RH = 100\%$, $\varepsilon_{ionomer} = 0.2$.

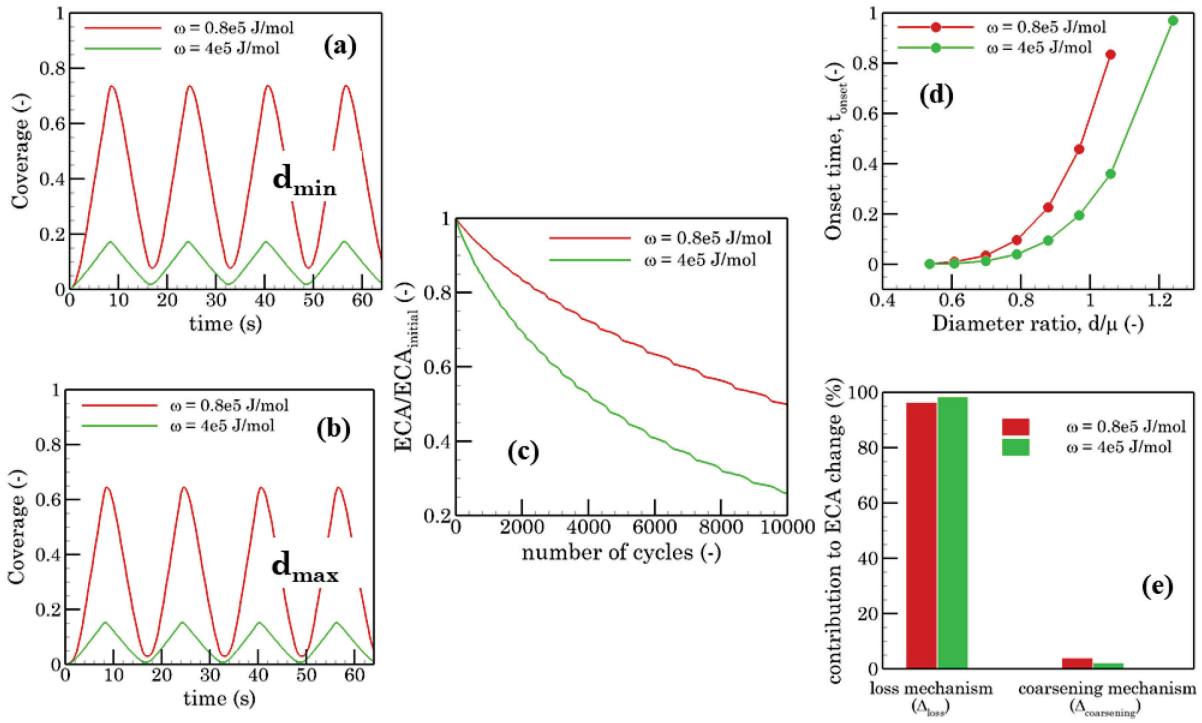

Fig. 6. Influence of platinum oxide-oxide interaction energy on potential-cycling induced degradation at high temperature and fully humidified conditions: Transient evolution of the oxide coverage for the initial four waveforms of the protocol have been shown for (a) minimum diameter and (b) maximum diameter of the distribution; (c) Electrochemical active area decay and (d) Dimensionless onset time and its dependence with normalized initial diameter bins at the two values of platinum oxide-oxide interaction energy, (e) Decoupling into loss and coarsening mechanisms that contribute to ECA change and its dependence on platinum oxide-oxide interaction energy. Conditions include a triangular wave potential cycling from 0.6-1.0 V for 10,000 cycles under H_2-Air condition at $T = 90^{\circ}C$, $RH = 100\%$, $\varepsilon_{ionomer} = 0.2$, $\mu = 2.8\ nm$.

Supporting Information

Mechanistic interactions in polymer electrolyte fuel cell catalyst layer degradation

Navneet Goswami[1], Jonathan B. Grunewald[2], Thomas F. Fuller[2], and Partha P. Mukherjee[1, *]

[1]School of Mechanical Engineering, Purdue University, West Lafayette, IN 47907, United States

[2]School of Chemical and Biomolecular Engineering, Georgia Institute of Technology, Atlanta, GA 30332, United States

*Corresponding author: pmukherjee@purdue.edu (P. P. Mukherjee)

S1. Sensitivity of parameters on a cyclic voltammogram profile:

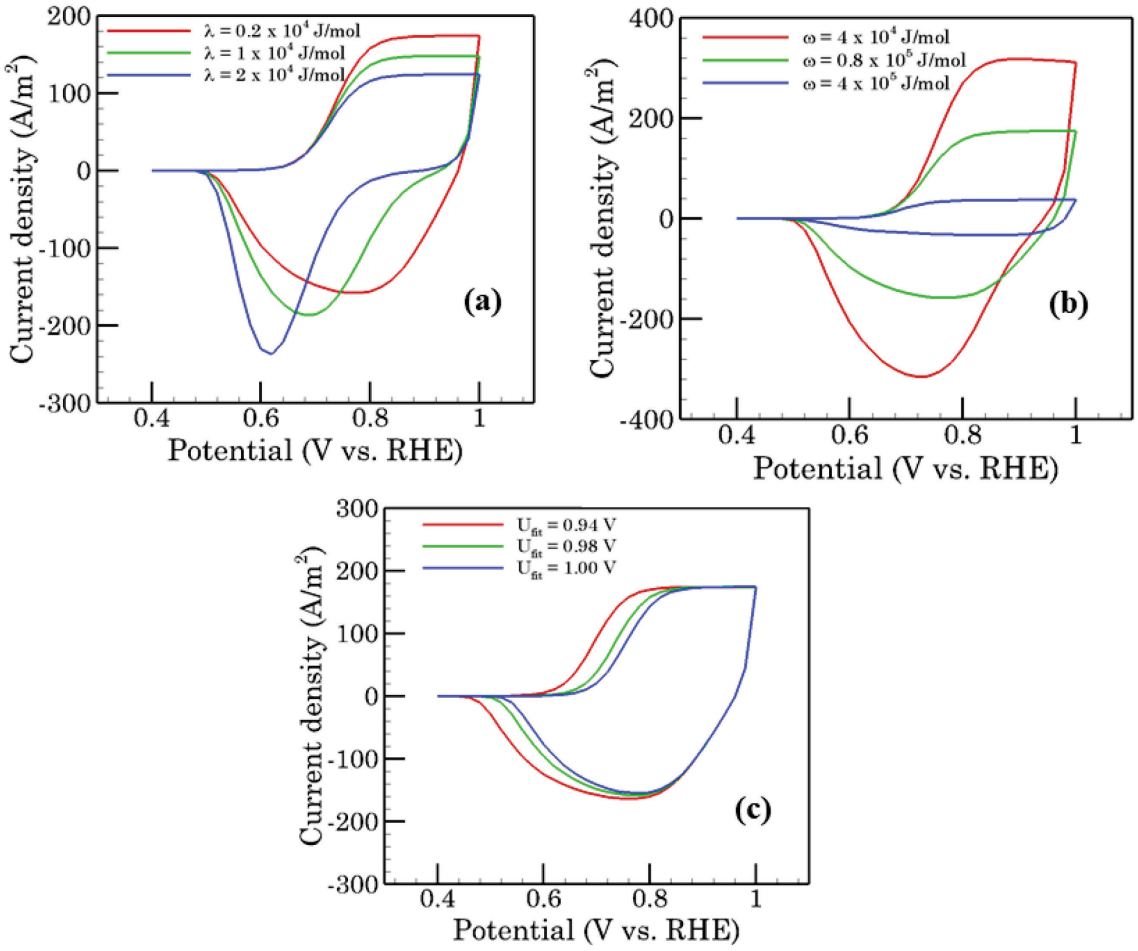

Fig. S1. Influence of kinetic parameters: (a) PtO-dependent kinetic barrier constant (λ), (b) Pt oxide-oxide interaction energy (ω), and (c) bulk equilibrium voltage for the onset of Pt-O formation (U_{fit}) on the shape of a cyclic voltammogram

The effect of thermo-kinetic parameters on the shape of a cyclic voltammogram (CV) corresponding to the initial durability cycle is shown in Fig. S1. The parameters of interest chosen in this analysis have been proved to majorly dictate the characteristics of a CV and emerge to be important while fitting to experimental data. Three values each of the PtO-

dependent kinetic barrier constant $\left(\lambda = 0.2\times10^4, 1\times10^4, 2\times10^4 \text{ J/mol}\right)$, Pt oxide-oxide interaction energy $\left(\omega = 4\times10^4, 0.8\times10^5, 4\times10^5 \text{ J/mol}\right)$, and bulk equilibrium voltage for the onset of Pt-O formation $\left(U_{fit} = 0.94, 0.98, 1 \text{ V}\right)$ have been considered. The baseline values $\left(\lambda = 0.2\times10^4 \text{ J/mol}, \omega = 0.8\times10^5 \text{ J/mol}, U_{fit} = 0.98 \text{ V}\right)$ constitute the curve with the best fit to the experimental CV data as seen in Fig. 2(a) in the main text. As observed in Fig. S1(a), tuning the PtO-dependent kinetic barrier constant to higher values decreases the anodic leveling current and shifts the cathodic peak towards the left, i.e., lower cathodic peak voltages and a higher absolute value of the cathodic peak currents. Change in the Pt oxide-oxide interaction energy (Fig. S1(b)) is manifested either in the form of expansion or contraction of the curve thereby changing the shape of the CV. Finally, bulk equilibrium voltage for the onset of Pt-O formation indicates the magnitude of the reversible open circuit potential (Fig. S1(c)) and accordingly modulates the point in the anodic half at which the oxidation of the catalyst particles is most likely to start (low value of U_{fit} means the early onset of PtO formation).

S2. Extraction of statistical parameters from an experimental particle size distribution (PSD):

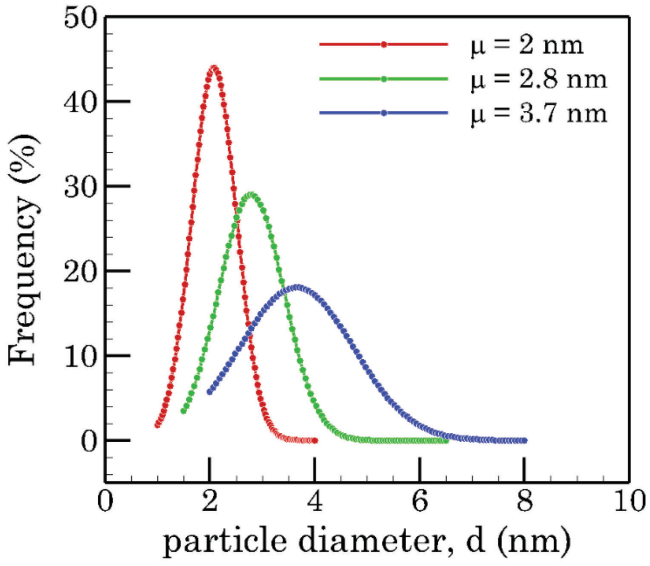

Fig. S2. The particle size distributions (PSDs) considered in the present study

An initial particle size distribution (PSD) serves as model input. The distribution consists of a finite number of particle groups, categorized by the particle radius and number density (number of particles) within each group. Based on an experimental transmission electron microscopy (TEM) dataset[1], analysis is performed to derive the relevant statistical parameters by fitting a Gaussian distribution. Fig. S2 shows the assumed PSD discretized into 100 groups with a mean particle radius (μ) of 2 nm (red curve), 2.8 nm (green curve), and 3.7 nm (blue curve),. The initial electrochemical active area (ECA) is assumed to be 55 m^2/g, which is the beginning of life ECA of the pristine membrane electrode assembly (MEA). At every time step, the particle groups are evolved (either coarsens or shrinks) as highlighted in the main text using the set of parameters enlisted in the Nomenclature section.

S3. Grid Independence test:

Results of the grid independence test are revealed in Fig. S3 which have been performed for a PSD with 2.8 nm mean particle radius, 20% ionomer volume fraction, and high temperature and fully humidified conditions (90°C and 100% respectively). It is observed that N = 25 (x-direction) and M = 100 (y-direction) can be deemed to be a suitable selection as it neither sacrifices the computation accuracy while maintaining a balanced computational overhead. All the simulation results presented in the manuscript are for the aforementioned grid.

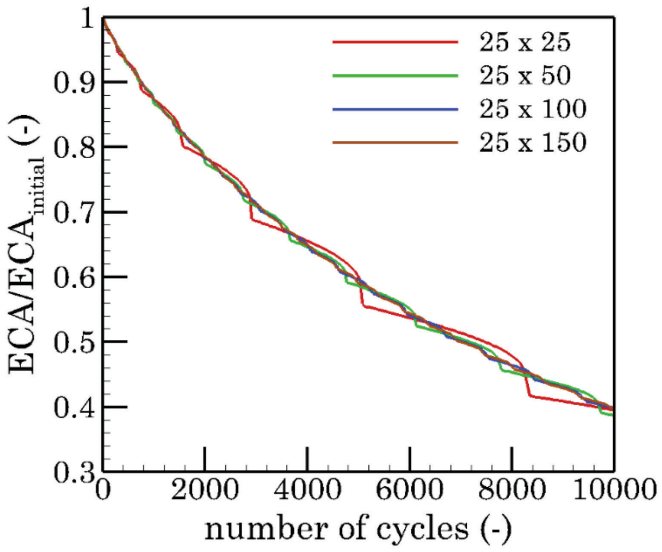

Fig. S3. Dependence of computational grid size on the transience of ECSA with cycling time

S4. Validation studies:

Fig. S4(a) shows the comparison of the simulated (from this work) and experimentally measured (from Bi and Fuller[2]) cathode cyclic voltammetry (CV) curves based on a potential cycle ranging from 0.4-1.0 V (vs. reference hydrogen electrode, RHE) with a scan rate of 50 mV/s at 60°C and fully humidified conditions. The CV current calculated as per Eq. S1 shows a good fit with that measured experimentally. The fitted thermo-kinetic parameters have been employed in all the simulations reported in this work. As seen in Fig. S4(b), the thermo-kinetic degradation model has been validated against experimental work of Harzer et al.[3] for triangular-wave potential cycling from 0.6-1.0 V under H_2-N_2 conditions for 10,000 cycles at 80°C and fully humidified conditions for two loading scenarios of the Pt catalyst - 0.1 and 0.4 mg/cm2. The simulation results accurately predict the transient profile of the change in ECA and mostly importantly, the loss in ECA after the end of 10,000 cycling sequences.

$$i = F\left(\pi d_{i,j}^2\right) Num_{i,j}\left(r_{net,Pt^{2+}} + r_{net,oxide}\right) L_{CCL} \tag{S1}$$

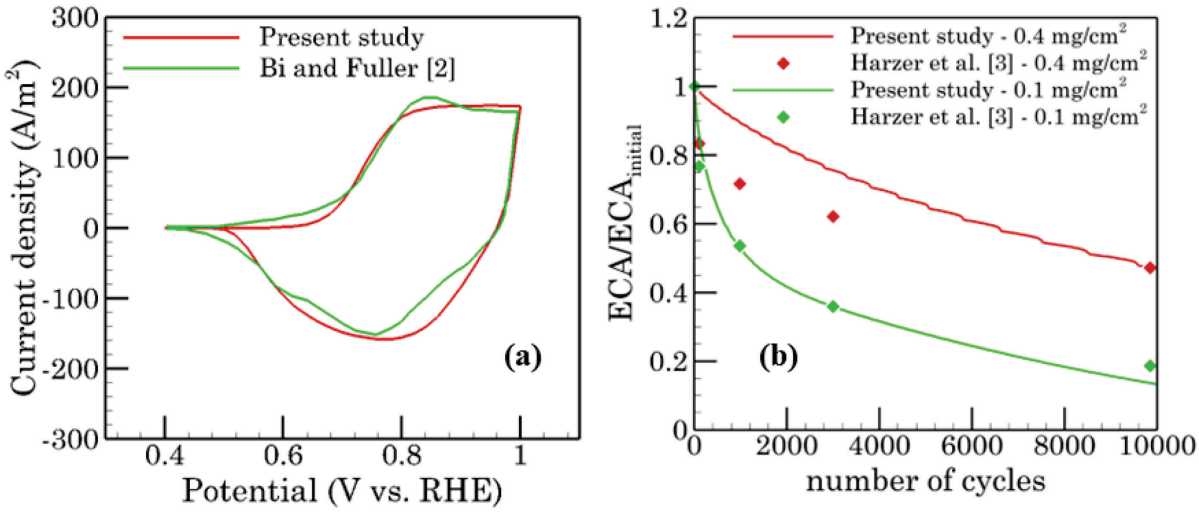

Fig. S4. Validation of the numerical code of the degradation model against literature data – (a) Cyclic Voltammetry (CV) profiles under 0.4-1.0 V potential cycling under H_2-N_2 conditions with Bi and Fuller[2], and (b) decay of electrochemical area under 0.6-1.0 V triangular-wave potential cycling under H_2-N_2 conditions for 10,000 cycles show agreement with Harzer et al.[3] for two loading scenarios of the Pt catalyst - 0.1 and 0.4 mg/cm^2

S5. Governing equations, boundary conditions employed in the reactive transport model:

Conservation of charge in Pt/C phase:

$$\frac{\partial}{\partial x}\left(\sigma_s^{eff}\frac{\partial \phi_s}{\partial x}\right) - j = 0 \tag{S2}$$

Conservation of charge in ionomer phase:

$$\frac{\partial}{\partial x}\left(\kappa_e^{eff}\frac{\partial \phi_e}{\partial x}\right) + j = 0 \tag{S3}$$

Conservation of gaseous oxygen in the pore phase:

$$\frac{\partial}{\partial x}\left(D_{\mathrm{O_2}} \frac{\varepsilon}{\tau} \frac{\partial c_{\mathrm{O_2}}}{\partial x} \right) + \frac{j}{4F} = 0 \tag{S4}$$

Conservation of water vapor in the pore phase:

$$\frac{\partial}{\partial x}\left(D_{\mathrm{H_2O}} \frac{\varepsilon}{\tau} \frac{\partial c_{\mathrm{H_2O}}}{\partial x} \right) - \frac{j}{2F} = 0 \tag{S5}$$

The system of coupled equations (S2-S5) needs to adhere to a set of boundary conditions as delineated below.

For the potential, ϕ_s in Pt/C phase:

$$\begin{aligned} &\text{Membrane-CCL interface } (x = 0) && \frac{\partial \phi_s}{\partial x} = 0 \\ &\text{CCL-GDL interface } (x = L_{CCL}) && -\sigma_s^{eff} \frac{\partial \phi_s}{\partial x} = I \end{aligned} \tag{S6}$$

For the potential, ϕ_e in ionomer phase:

$$\begin{aligned} &\text{Membrane-CCL interface } (x = 0) && -\kappa_e^{eff} \frac{\partial \phi_e}{\partial x} = I \\ &\text{CCL-GDL interface } (x = L_{CCL}) && \frac{\partial \phi_e}{\partial x} = 0 \end{aligned} \tag{S7}$$

For the concentration of gaseous oxygen, $c_{\mathrm{O_2}}$ in the pore phase:

$$\text{Membrane-CCL interface } (x = 0) \qquad \frac{\partial c_{\mathrm{O_2}}}{\partial x} = 0 \tag{S8}$$

CCL-GDL interface $(x = L_{CCL})$ $$c_{O_2} = c_{O_2}\Big|_{x=L_{CCL}}$$

For the concentration of gaseous oxygen, c_{H_2O} in the pore phase:

Membrane-CCL interface $(x = 0)$ $$-D_{H_2O}\frac{\varepsilon}{\tau}\frac{\partial c_{H_2O}}{\partial x} = N_{w,net}\Big|_{x=0} \quad \text{(S9)}$$

CCL-GDL interface $(x = L_{CCL})$ $$c_{H_2O} = c_{H_2O}\Big|_{x=L_{CCL}}$$

The oxygen concentration at the CCL–GDL interface ($x = L_{CCL}$) can be calculated by taking into account the drop from the constant gas concentration in the gas channel through the diffusion resistance in the GDL.

$$c_{O_2}\Big|_{x=L_{CCL}} = c_{O_2,\,inlet} - \frac{I}{4F}\frac{L_{GDL}}{\left(D_{O_2}\frac{\varepsilon}{\tau}\right)_{GDL}} \quad \text{(S10)}$$

Gaseous oxygen ingresses through the secondary pores and finally penetrates through the thin ionomer film (thickness is denoted as $\hat{t}$) that covers the catalyst particles and consequently observes a local diffusion resistance. A concentration jump exists at the pore-ionomer interface due to the application of Henry's law as seen in Eq. S11. The oxygen reaching the available reaction sites can be calculated using Eq. S12 by including the effect of the film resistance offered by the ionomer.

$$c_{O_2}^{ionomer\ surface} = \frac{c_{O_2}}{H_{O_2}} \tag{S11}$$

$$c_{O_2}^{reaction\ site} = c_{O_2}^{ionomer\ surface} - \left(\frac{I}{4F}\right)\left(\frac{\hat{t}}{D_{O_2}^{ionomer}}\right) \tag{S12}$$

It must be pointed out that the bulk value of proton conductivity of the ionomer phase $\left(\kappa^{bulk}\right)$ (units of S/m), Henry's constant $\left(H_{O_2}\right)$ (units of Pa-m^{3}mol^{-1}), and oxygen diffusivity through the ionomer $\left(D_{O_2}^{ionomer}\right)$ (units of m^2/s) are a function of water content (λ) which further depends on the water activity, *a*, as per the experimental correlation shown in Eq. S16.

$$\kappa_e^{bulk} = 100\exp\left[1268\left(\frac{1}{303}-\frac{1}{T}\right)\right]\left(0.005139\lambda - 0.00326\right) \tag{S13}$$

$$D_{O_2}^{ionomer} = 1.3926\times10^{-10}\,\lambda^{0.708} e^{\left\{\frac{T-273.15}{106.65} - 1.6461\times10^{-10}\lambda^{0.708} + 5.2\times10^{-10}\right\}} \tag{S14}$$

$$H_{O_2} = 0.1552 e^{\left(14.1 + 0.0302\lambda - \frac{666}{T}\right)} \tag{S15}$$

$$\lambda = \begin{cases} 0.043 + 17.81a - 39.85a^2 + 36a^3 & \text{for } 0 < a \le 1 \\ 14 + 1.4\left(a-1\right) & \text{for } 1 < a \le 3 \end{cases} \tag{S16}$$

The water activity, *a* depends on the local variation of water vapor concentration within the CCL and can be approximated as:

$$a = \frac{c_{H_2O}}{c_{H_2O}^{sat}} \tag{S17}$$

A balance between the fluxes resulting from electro-osmotic drag and back diffusion gives the net water flux at the membrane-CCL interface ($x = 0$) in Eq. S18. In this work, the magnitude of the water transport coefficient (α) is considered as 0.2. Invoking the diffusion resistance through the GDL, the concentration for water vapor at the CCL-GDL boundary ($x = L_{CCL}$) can be evaluated (Eq. S19). The net water flux at the CCL-GDL interface (Eq. S20) can be determined by adding the generation term to the interfacial flux in Eq. S18.

$$N_{w,net}\Big|_{x=0} = N_{w,electroosmotic\ drag} - N_{w,back\ diffusion} = \alpha \frac{I}{F} \tag{S18}$$

$$c_{\mathrm{H_2O}}\Big|_{x=L_{CCL}} = c_{\mathrm{H_2O},\ inlet} + \quad N_{w,net}\Big|_{x=L_{CCL}} \frac{L_{GDL}}{\left(D_{\mathrm{H_2O}} \frac{\varepsilon}{\tau}\right)_{GDL}} \tag{S19}$$

$$N_{w,net}\Big|_{x=L_{CCL}} = N_{w,net}\Big|_{x=0} + N_{w,production} = \alpha \frac{I}{F} + \frac{I}{2F} = (2\alpha + 1)\frac{I}{2F} \tag{S20}$$

The mole fractions of the multi-component species in addition to their corresponding concentration values at the channel inlet can be computed based on the operating conditions (relative humidity, pressure, temperature) as highlighted in Eqs. (S21-S27).

$$c_{\mathrm{H_2O},\ inlet} = RH.c^{sat}_{\mathrm{H_2O}} \tag{S21}$$

$$c^{sat}_{\mathrm{H_2O}} = \frac{p^{sat}_{\mathrm{H_2O}}}{RT} \tag{S22}$$

$$\sum x_i = 1 \tag{S23}$$

$$x_{H_2O} = RH.\frac{p^{sat}_{H_2O}}{p} \tag{S24}$$

$$x_{O_2} = 0.21\left(1 - x_{H_2O}\right) \tag{S25}$$

$$x_{N_2} = 0.79\left(1 - x_{H_2O}\right) \tag{S26}$$

$$c_{O_2,\,inlet} = x_{O_2}\frac{p}{RT} \tag{S27}$$

In this study, the combined diffusion coefficients of gaseous oxygen and water vapor (Eq. S28) are based on a harmonic averaging of the coefficients arising from Knudsen diffusion (as per Eq. S29) and Binary diffusion (as per Eq. S30). The reference pressure (p_o) and reference temperature (T_o) are taken as 1 atm and 273 K respectively.

$$D_i = \left(\frac{1}{D_{K,i}} + \frac{1}{D^g_{b,i}}\right)^{-1} \tag{S28}$$

$$D_{K,i} = \left(\frac{2}{3}\right)\left(\frac{8RT}{\pi M_k}\right)^{\frac{1}{2}} r_p \tag{S29}$$

$$D^g_{b,i}\left(T,p\right) = D^g_{b,i,o}\left(\frac{T}{T_o}\right)^{\frac{3}{2}}\left(\frac{p_o}{p}\right) \tag{S30}$$

The correlation for exchange current density in addition to bulk values of diffusivities and electronic conductivity have been taken from Goswami et al.[4]

S6. Evolution of the particle size distribution (PSD):

The particle size distribution in the form of number density, or equivalently, the number of particles per unit volume have been displayed for the pristine and EOL electrode for two scenarios – (a) 80°C, 60% RH (similar conditions as in Figure 2 of the manuscript) and, (b) 60°C, 20% RH. The broadening of the PSD towards the left at the EOL stage reveals the dissolution dependence of the particle diameters towards a limiting case where the number density drops to zero (Eq. 30 from the manuscript). Further, the inset figures also show that the PSD slightly shifts towards the right with the tail approaching larger particle sizes which is a manifestation of the redeposition phenomena that results in particle coarsening. It must also be mentioned that the particle coarsening is a bit more prominent under low humidity conditions (scenario (b)). Furthermore, when compared to coarsening, dissolution is the more significant degradation mode also observed in Baroody and Kjeang[5].

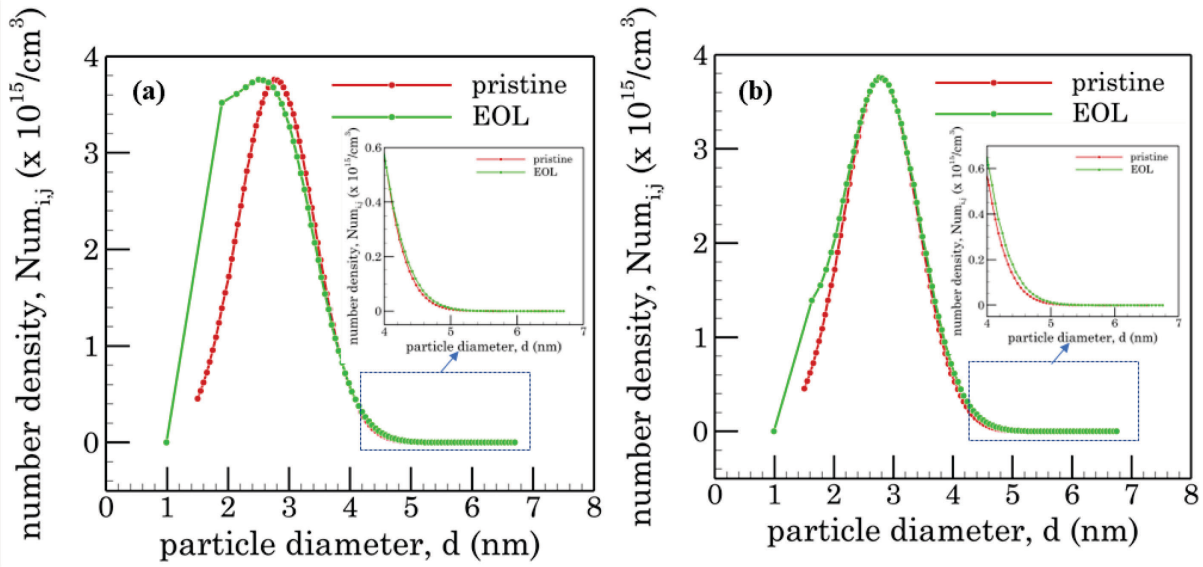

Fig. S5. The particle size distributions (PSDs) for the pristine and EOL electrode for two scenarios – (a) 80°C, 60% RH and, (b) 60°C, 20% RH

Nomenclature:

Symbol	Quantity	Description
ν_1	1.0×10^4 Hz	dissolution attempt frequency
ν_2	6.0×10^6 Hz	forward/backward dissolution rate factor
Γ	2.2×10^{-9} mol/cm^2	platinum surface site density
$\bar{H}_1$	4.7×10^4 J/mol	platinum dissolution activation enthalpy under fully humidified conditions
β_1	0.5	Butler−Volmer transfer coefficient for Pt dissolution
n_1	2	electrons transferred during Pt dissolution
$c_{Pt^{2+}}^{ref}$	1.0 mol/L	reference Pt^{2+} concentration
U_{eq}	1.188 V	thermodynamic bulk equilibrium voltage for platinum dissolution
ν_1^*	14.0×10^4 Hz	forward platinum oxide formation rate constant
ν_2^*	16.0×10^{-2} Hz	backward platinum oxide formation rate constant
$\bar{H}_2$	1.8×10^4 J/mol	partial molar oxide formation activation enthalpy (zero coverage)
$\beta_{2,a}$	0.5	anodic transfer coefficient for platinum oxide formation
$\beta_{2,c}$	0.35	cathodic transfer coefficient for platinum oxide formation
n_2	2	electrons transferred during platinum oxide formation
pH	0	system pH
λ	0.2×10^4 J/mol	platinum oxide-dependent kinetic barrier constant
U_{fit}	0.98 V	thermodynamic bulk equilibrium voltage for platinum oxide formation
ω	0.8×10^5 J/mol	platinum oxide−oxide interaction energy
γ_{Pt}	2.37×10^{-4} J/cm^2	surface tension of platinum
γ_{PtO}	1.0×10^{-4} J/cm^2	surface tension of platinum oxide
Ω_{Pt}	9.26 cm^3/mol	molar volume of platinum
Ω_{PtO}	14.97 cm^3/mol	molar volume of platinum oxide
ρ_{Pt}	21.09 cm^3/mol	density of platinum
$D_{Pt^{2+}}$	4.0×10^{-6} cm^2/s	diffusion coefficient of Pt^{2+} through the ionomer
L	10 μm	electrode thickness
T	60°C/ 80°C/ 90°C	Temperature
RH	20%/ 60%/ 100%	Relative humidity
$\varepsilon_{ionomer}$	0.1/ 0.15/ 0.20	volume fraction of the ionomer

List of Abbreviations:

PEFC	Polymer Electrolyte Fuel Cell
Pt	Platinum
ORR	Oxygen Reduction Reaction
ECA	Electrochemical Active Area
AST	Accelerated Stress Test
RH	Relative Humidity
MEA	Membrane Electrode Assembly
PSD	Particle Size Distribution
UPL	Upper Potential Limit
CCL	Cathode Catalyst Layer
GDL	Gas Diffusion Layer
GSA	Geometric Surface Area
EOL	End Of Life
CV	Cyclic Voltammetry

References:

1 D. J. S. Sandbeck, D. J. S. Sandbeck, M. Inaba, J. Quinson, J. Bucher, A. Zana, M. Arenz, M. Arenz and S. Cherevko, *ACS Applied Materials and Interfaces*, 2020, **12**, 25718–25727.

2 W. Bi and T. F. Fuller, *Journal of Power Sources*, 2008, **178**, 188–196.

3 G. S. Harzer, J. N. Schwämmlein, A. M. Damjanović, S. Ghosh and H. A. Gasteiger, *Journal of The Electrochemical Society*, 2018, **165**, F3118–F3131.

4 N. Goswami, A. N. Mistry, J. B. Grunewald, T. F. Fuller and P. P. Mukherjee, *Journal of The Electrochemical Society*, 2020, **167**, 084519.

5 H. A. Baroody and E. Kjeang, *Journal of The Electrochemical Society*, 2021, **168**, 044524.